Dynamic Albedo Modelling for Bifacial FPVs

MSc Thesis Project Report

Ricardo Velásquez Diaz 6279112

Delft University of Technology

TU Delft

Dynamic Albedo Modelling for Bifacial FPVs

MSc Thesis Project Report

by

Ricardo Velásquez Diaz 6279112

Thesis Supervisor: Rudi Santbergen
Daily Supervisor: Sathya Shanka Vasuki.
Faculty: Faculty of Electrical Engineering, Mathematics and Computer Science Delft

TU Delft

Preface

After several years working in the industrial sector in Chile, deciding to continue my studies was not an easy choice. However, my enthusiasm for renewable energy became the driving force that led me far from my homeland to the Netherlands. Despite the challenges I faced along the way, I am now certain that it was the right decision. This thesis represents the culmination of my academic journey and the beginning of a new chapter, where I hope to contribute, in my own small way, to a more sustainable and greener future.

Conducting research in an international academic environment has been an inspiring and enriching experience. Meeting people from all around the world who share a common goal of contributing to a more sustainable energy scenario inspires me to keep working in this field. I would like to express my sincere gratitude to my daily supervisor, Sathya, for his continuous guidance and for always taking the time to answer my questions whenever I felt uncertain about my direction. I would also like to thank Dr Rudi Santbergen for the instances of discussion about my project and his constructive feedback to conduct my research properly.

Finally, I want to thank my family, my friends in Chile, and all the new friends I made during my stay in the Netherlands. Every laugh, every run, and every short or long conversation helped me to reach this point without losing my balance.

I hope that the findings presented in this work contribute to the ongoing research in the field of offshore photovoltaics and serve as a valuable reference for future students who share an interest in this promising area that continues to grow every year.

Ricardo Velásquez Diaz | *6279112*
Delft, February 2026

Summary

Ocean surface albedo (OSA) is the fraction of incoming solar radiation reflected back by the ocean surface, driven mainly by wave geometry, whitecaps, and subsurface components like chlorophyll and mineral particles. The accurate modelling of this parameter is from importance for offshore floating photovoltaics (OFPV), where the bifacial panels can be used to boost the energy yield, impacting the levelized cost of electricity (LCOE) and energy transition strategies.

Current albedo datasets lack accuracy when considering OSA as a constant value, which is an oversimplification that ignores the sea dynamics. Moreover, the spatial resolution of these sources is commonly 1/24° (about 4km), which is a coarse resolution considering that the characteristic length scale of an OFPV plant is in the order of 1km. Empirical models focused specifically on OSA modeling exhibit an improvement compared to the existing datasets; however, they fall short by not including all the parameters that effectively influence OSA, and their empirical nature, which makes their accuracy location-specific. This thesis addresses these gaps, developing and validating a model based on GenPro4 to estimate OSA in realistic ocean scenarios.

The proposed model was tested in two main waterbodies classes: clear and turbid waters, to analyze and determine its accuracy under these two opposite sea states. Root mean square errors (RMSE) values of 0.72% for clear and 3.8% for turbid waters confirmed its robustness and reliability. Furthermore, a sensitivity analysis was executed to identify the key parameters that affect the bifacial gain when considering the dynamic nature of OSA, finding that sea roughness (waves geometry) defined by the significant height wave (H_s) and its peak period (T_p), had a significant effect, producing bifacial gain changes close to 3.5% between calm cases and rough wave scenarios.

Finally, regional simulations on four locations across the globe revealed that despite seasonal variations of bifacial gain, an annual average value ranging from 5 to 8% is obtained regardless of the specific location of the OFPV plant. These findings confirm that bifacial gain varies with different sea states but remains within a predictable and practical range for OFPV design and performance assessment.

Economically, this 5–8% yield uplift offsets the additional CAPEX from bifacial panels, potentially achieving breakeven or lower LCOE values compared to monofacial cases. Dynamic OSA thus drives bifacial viability, confirming competitive OFPV performance across oceans.

Contents

Nomenclature

Abbreviations

Abbreviation	Definition
BIOSOPE	Biogeochemistry and Optics South Pacific Experiment
BRDF	Bidirectional Reflectance Distribution Function
CAPEX	Capital Expenditures
CDOM	Coloured Dissolved Organic Matter
CERES	Clouds and the Earth's Radiation Energy System
COVE	CERES Ocean Validation Experiment
ECMWF	European Centre for Medium-Range Weather Forecasts
JONSWAP	Joint North Sea Wave Project
LUT	Look Up Table
OFPV	Offshore Floating Photovoltaics
OPEX	Operations Expenditures
NAP	Non-Algal Particles
NASA	National Aeronautics and Space Administration
OSA	Ocean Surface Albedo
RMSE	Normalized Root Mean Squared Error
TSM	Total Suspended Matter

Symbols

Symbol	Definition	Unit
a_t	Overall Absorption Coefficient	m^{-1}
a_{bp}	Bioproduct Absorption Coefficient	m^{-1}
a_d	CDOM Absorption Coefficient	m^{-1}
a_g	Non-algal Absorption Coefficient	m^{-1}
a_{ph}	Phytoplankton Absorption Coefficient	m^{-1}
a_w	Water Absorption Coefficient	m^{-1}
α_{bp}	Bioproduct Albedo	-
α_{TSM}	Total Suspended Matter Albedo	-
α_{wc}	Whitecap Albedo	-
A	Absorption	-
A_{wc}	Whitecap Coverage Area	m^2
b_b	Overall Backscattering Coefficient	m^{-1}
b_{bp}	Mineral Particles Backscattering Coefficient	m^{-1}
b_{bw}	Water Backscattering Coefficient	m^{-1}

Table 1 (continued)

Symbol	Definition	Unit
E_d	Downwelling Radiation	W/m^2
$E(f,\theta)$	Energy Density Spectrum of a Wave	
E_u	Total Upwelling Irradiance	W/m^2
f_{dif}	Diffuse Fraction of Total Incident Radiation	-
f_{dir}	Direct Fraction of Total Incident Radiation	-
f_{wc}	Whitecap Coverage Fraction	-
k	Imaginary Part of Refractive Index	-
k_x	Wave Number in x Coordinate	m^{-1}
k_y	Wave Number in y Coordinate	m^{-1}
n	Real Part of Refractive Index	-
$[Chl]$	Chlorophyll Concentration	mg/m^3
λ	Wavelength	nm
R^2	Coefficient of Determination	-
R	Reflectivity	-
σ	Sea Roughness	-
θ	Zenith Angle	rad
θ_i	Incidence Angle	rad
θ_t	Transmission Angle	rad
T	Transmission	-
U_{10}	Wind Speed Velocity at 10m Over Surface	m/s
ω	Angular Frequency	rad/s

1

Introduction

1.1. Why to model albedo in waterbodies?

Solar energy is one of the main driving forces to reach a greener energy matrix. However, this energy type has to compete for land usage with other activities such as agriculture or construction. In this context, Offshore Floating Photovoltaics (OFPV) emerges as an ideal solution, as there is a vast space in the oceans to build these types of projects. Nevertheless, it is important to consider that in such a case, operating conditions are different and, therefore, the analytical approach must be adapted to consider the new environmental conditions.

Sea dynamics will affect the performance of the PV plant in terms of mechanical stability, temperature operation, and total reflected radiation reaching the PV module. The latter is of importance because the presence of a dynamic profile shaped by the movement of waves and the intermittent generation of foam produced by breaking waves will alter the albedo in that zone, making it a time-and-space dependent variable that varies the amount of radiation directed upwards once reflected from the surface of the ocean.

Due to its relevance in radiative transfer, albedo over waterbodies like seas, lakes, oceans, among others, has caught the attention of several researchers in recent decades. Several approaches have been proposed over the years. However, the resulting models lack accuracy as they do not contemplate all the factors present in the water surface dynamics, and often they just consider the ocean surface albedo (OSA) as a constant (OSA = 0.06) when simulating the performance of PV modules [1]. The stochastic nature of waterbodies introduces heterogeneity that challenges the assumption of a constant albedo, and, when studying the optical properties of the air-water interface, its irregular roughness and heterogeneous composition must be considered.

OFPV presents numerous advantages compared to on-land conventional PV plants. In the specific case of the dynamic behavior of albedo, the textured surface of the sea can be utilized to harvest more energy by the use of bifacial PV modules. Several pilot plants have been constructed to measure the difference in energy yield (EY) between both types of PV modules, monofacial and bifacial. In particular, an OFPV pilot plant tested in Frankfurt, Germany, reported a bifacial gain (BG) of almost 13.5% [2] calculated based on Equation 1.1.

$$BG = \frac{EY_{BF} - EY_{MF}}{EY_{MF}} \tag{1.1}$$

Although OFPV was initially conceived as a solution to the increasing scarcity of land space, it also offers distinct optical advantages over conventional PV plants. One of the main advantages is the potential increase in the energy yield of such plants because of the larger and dynamic albedo present on waterbodies. Therefore, this study aims to provide deeper insight into the behavior of this variable to understand the real extent of its effect in energy yield calculations of OFPV.

In the following chapter, a review of previous studies regarding waterbody albedo is discussed to provide a comprehensive background on the phenomenon. After this review, it will be possible to identify existing gaps in the current state of the art and set the research questions that will be addressed in this thesis.

1.2. Literature Review

The surface of waterbodies considers liquid water as well as whitecaps (foam) created by waves. However, those are not the only factors affecting albedo. Subsurface components, such as bioproducts or suspended material dissolved in water, also impact in an important extent the total radiation reflected from the waterbody. Several studies related to OSA are reviewed in [3], identifying three key factors that influence albedo:

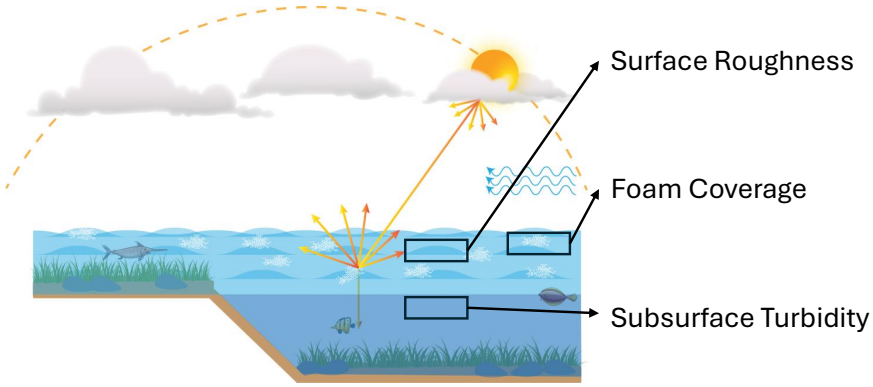

Figure 1.1: Identification of main factors that influence ocean surface albedo. Modified from [3]

These factors contribute to the total albedo of a waterbody. However, their modeling remains an open research question, as no consensus has yet been established on how to integrate the three factors into a unified predictive model.

1.2.1. Factors that affect albedo

Foam Coverage

Whitecaps and streaks, also known as sea foam, may occupy a small fraction of a waterbody, but their presence alters reflectivity measurements significantly. Even coverage percentages as low as 4% can double OSA at low zenith angles compared to foam-free sea [4]. Consequently, numerous investigations have analyzed the influence of foam on OSA and also how to model it. Montecarlo simulations stand out when modeling this type of phenomenon, as they effectively account for the stochastic nature of solar radiation. Despite the accuracy of certain methods like ray tracing or Montecarlo simulations, their high computational cost generates the need to look for a different approach.

Empirical models consider foam as an isotropic medium, with an albedo assumed constant across the entire whitecap. The spectral value of this parameter ($\alpha_{wc}(\lambda)$) is treated as a polynomial based on absorption coefficients of water ($a_w(\lambda)$), as it is mostly a mix of water and air [5], as shown in Equation 1.2.

$$\alpha_{wc}(\lambda) = \frac{0.5}{100} \cdot (60.063 - 5.127 \cdot x + 2.799 \cdot x^2 - 0.713 \cdot x^3 + 0.044 \cdot x^4 \tag{1.2}$$

Where $x = ln(a_w(\lambda))$. The validity of this model has been evaluated through experimental measurements, which have suggested modifications to the existing parametrization [6–8]. Nevertheless, these modifications are generally region-specific, as they account for geographical conditions. As a result, Equation 1.2 remains the standard method to estimate whitecap albedo.

The methodology for simulating whitecap coverage relies, in most cases, on visual recognition of ocean satellite imagery, where white zones in the pictures are distinguished, and a numerical model that fits such data is established [1, 9, 10]. The main factor influencing foam coverage (f_{wc}) in waterbodies is wind speed (U_{10}). Exponential growth models are typically used to describe this relationship over a specific range of wind speeds, as expressed in Equation 1.3, where c_1 and c_2 are empirical parameters

$$f_{wc} \propto c_1 \cdot U_{10}^{c_2} \tag{1.3}$$

Additionally, satellite-based radiometric observations support exponential relationships in the wind speed range 3-20 m/s [11–13], validating the dependence between both variables.

Subsurface Turbidity

Considering the sea, representing it merely as a mixture of water and foam is an overly simplistic approach. Phytoplankton and inorganic mineral particles also affect OSA, as these organisms interact with solar radiation primarily in the range 400-700 nm [14]. A complete model must therefore account for inherent water properties as well as the organic and inorganic components present in it. Two major factors often characterize water clarity: **chlorophyll concentration ([Chl])** and **total suspended matter (TSM)**. The importance of these factors mainly depends on the waterbody under study.

Investigators in [15] analyzed a total of 18 lakes with 52 sampling sites in Northeast China, obtaining a relationship between OSA and TSM with a coefficient of determination R^2 = 0.8484. Despite this good sign of correlation, albedo is influenced by multiple interacting factors, rather than by simple univariable relationships. For instance, TSM effects on OSA are modulated by zenith angle and wind, even when TSM concentration remains constant [16].

The upper few meters of a waterbody are crucial to analyze the biophysical processes that influence OSA, where chlorophyll is the primary parameter in these studies. As bioproducts are immersed in the subsurface, their absorption (a_{bp}) and backscattering coefficients (b_{bbp}) play an important role on albedo [17]. Both expressions can be modeled as a function of chlorophyll concentration and wavelength [18], with datasets available in the existing literature. Then, the albedo contribution coming from the organic component α_{bp} can be considered as follows.

$$\alpha_{bp} = f(\lambda, [Chl], a_w, a_{bp}, b_w, b_{bbp}) \tag{1.4}$$

Where the coefficients a_w and b_w correspond to the absorption and backscattering coefficient of water, respectively, and [Chl] is the chlorophyll concentration.

Sea Roughness

As it was discussed before, considering a fixed albedo for sea surfaces, like on-land PV plants, is a risky assumption due to the wavy profile intrinsic to the sea. For many years, a conservative value of 0.06 was used to model OSA in waterbodies. Nevertheless, OSA can change in a range from 0.01 to 0.40 during the day due to the change of zenith angle [19].

Oceanographic studies have proposed different methods to simulate sea motion. In a simplistic vision, sea motion can be classified into two main components. First, irregular waves are generated by the wind effect existing a relationship between the two variables. Second, waves with longer lengths, known as swells, have travelled away from distant storms; they move independently from local weather and wind, maintaining a steady, long wavelength [20].

Although there are several models to simulate sea roughness, like The Joint North Sea Wave Project (JONSWAP) [21], they are specific to a certain sea regime, lacking accuracy when being applied to waterbodies with different oceanic conditions. Then, it is necessary to follow a different approach, more generic, to avoid location-dependencies of the phenomenon. Every sea state can be represented as a sum of different harmonic sea waves. These harmonic waves will be represented by a specific amplitude (H) and a period associated with it (T). Therefore, by considering a mean or general value of those two parameters, it is possible to describe the wave spectra in energy terms.

A significant height of the wave (H_s) and a peak period (T_p) are two parameters often registered in wave measurements [22]. Such parameters have associated a unique energy density spectrum ($E(f, \theta)$) inherent to a specific wave regime. The energy density spectrum exists as a function of frequency and directional spread. As we are working in a 3D space, the coordinates of frequency (f, θ) must be adapted and redefined for a 2D Cartesian plane (x, y). The variable to do that is the wave number, as it relates both variables in the spectrum.

Then, for a certain 2D space of dimensions L_x and L_y discretized in N_x and N_y points, the following grid map is defined.

$$k_x = \frac{(\frac{-N_x}{2} : \frac{N_x}{2} - 1)}{L_x} \tag{1.5}$$

$$k_y = \frac{(\frac{-N_y}{2} : \frac{N_y}{2} - 1)}{L_y} \tag{1.6}$$

Analogously, for the frequency spectra, the wave number is defined as follows.

$$k_f = \frac{(2 \cdot \pi \cdot f)^2}{g} \tag{1.7}$$

$$k_{x,f} = k_f \cdot cos(\theta) \tag{1.8}$$

$$k_{y,f} = k_f \cdot sin(\theta) \tag{1.9}$$

In reality, k_x and $k_{x,f}$ (k_y and $k_{y,f}$) rarely match; it is necessary to find the closest point of the wave number in the frequency spectra to be assigned to its counterpart in the cartesian plane. Once this value is found, the energy spectrum is assigned to the pair (k_x, k_y). This originates an amplitude value for the wave (Ψ), and then, if we consider a 2D cartesian map discretized in m points in the x coordinate and n points in the y coordinate, the wave height map is calculated as follows.

$$\eta(x, y) = \sum_{m,n} \Psi_{mn} \cos(k_{x,mn}x + k_{y,mn}y + \phi_{mn}) \tag{1.10}$$

Equation 1.10 is a Fourier series of superposed harmonic waves, which will give as a result the wave height spectrum of the sea represented by the variable η [23].

1.2.2. Current OSA Sources

The complexity of including all relevant parameters discussed above in a single mathematical model makes the computation challenging. For this reason look-up tables (LUT) have been proposed [24]; nonetheless, their limited extrapolation capability reduces their utility for albedo analysis. Some other albedo simulation programs use apparent color radiometry from satellite data to estimate OSA. Again, this technique is not the best option because the distance between nodes is several kilometers, and a typical PV farm scale has a characteristic length of less than 1 kilometer. Then, an analytical approach based on the factors discussed in the previous section is the most suitable approach because it can be applied to length scales smaller than the distance between two nodes in satellite-based maps.

Nowadays, it is possible to obtain datasets of albedo over the sea [25]. These datasets are generated based on satellite observations and algorithms that use input parameters, including zenith angle, wind speed, chlorophyll content, wind direction, and others, to produce a bidirectional reflectance distribution function (BRDF). Online repositories of historical, current, and forecast data for weather parameters, including albedo, are available for use. Copernicus Marine Service - ECMWF [22] offers worldwide maps with a resolution of 1/12°, but it can be finer up to 1/24° or 1/72° in specific regions. NASA Earthdata [26] is another dataset that offers a resolution as low as 500 m, but with limited coverage areas. **The coarse spatial resolution of these datasets constitutes a limitation for deriving OSA with sufficient accuracy for OFPV modelling.**

Because datasets are unreliable sources, two analytical models are examined in this chapter to assess their strengths and limitations for simulating OSA. Despite their different approaches, all of them follow an identical procedure to obtain the albedo given by Equation 1.11, Equation 1.12 and Equation 1.13

$$OSA_{dir} = (\alpha_{w,dir} + \alpha_{bp,dir}) \cdot (1 - f_{wc}) + \alpha_{wc} \cdot f_{wc} \tag{1.11}$$

$$OSA_{dif} = (\alpha_{w.dif} + \alpha_{bp,dif}) \cdot (1 - f_{wc}) + \alpha_{wc} \cdot f_{wc} \tag{1.12}$$

$$OSA = OSA_{dir} \cdot f_{dir} + OSA_{dif} \cdot f_{dif} \tag{1.13}$$

The two models are discussed below.

1.2.3. Golroodbari Model

This model accounts for both direct and diffuse components of solar radiation, as well as the contribution of water and whitecaps in the analysis [1]. While the solar zenith angle is commonly the main parameter when studying albedo, this model also incorporates the effect of wind, ocean roughness, and atmospheric and oceanic properties to calculate the albedo of a waterbody. None of these parameters have a linear effect on albedo, and their interactions can modulate the influence of one another. Consequently, in this study, OSA is considered as a multivariable function, whose value is obtained as the sum of two main contributions: **Whitecaps** and **Water surface**.

The albedo of whitecaps is calculated using Equation 1.2 while the whitecap coverage is obtained with Equation 1.14.

$$f_{wc} = 3.97 \cdot 10^{-2} \cdot U_{10}^{1.59} \tag{1.14}$$

The values of the absorption coefficient of water used in Equation 1.2 are extracted from [27], and the total value is divided by two, as experimental evidence indicates that whitecap fractions tend to be approximately half of that of dense foam [5].

The main advantage of this model lies in its simplicity. The data needed to perform the calculations are widely available, and the simplifications used make the calculations simpler and therefore faster.

However, such assumptions introduce limitations that reduce the physical realism of the model. First, representing sea surface roughness just as a function of wind speed is not an accurate approach. The actual sea surface topology is the result of the combination of locally wind-generated waves and swells, the latter being highly independent of local wind conditions. Then, describing roughness exclusively through wind speed fails to capture the complete nature of the phenomenon.

Secondly, and most importantly, the analysis only contemplates the surface of the waterbody (whitecap and water), but it ignores the contribution of the subsurface. The dynamic of the underlying layer strongly affects OSA. The variations in water colour are direct evidence of these subsurface effects. Hence, the inclusion of subsurface optical interactions is essential for achieving a more comprehensive representation of OSA.

1.2.4. Séférian Model

Although waves and whitecaps play an important role in obtaining realistic OSA values, simplifying the calculation to only these two factors gives a limited picture of the phenomenon. Subsurface elements interact with light coming from the sun, producing absorption, backscattering, and reflection.

This second model proposes a more comprehensive approach by considering the contribution of organisms present in waterbodies [28]. In particular, the Séférian study adds the existence of phytoplankton to the main analysis measured as chlorophyll concentration in the subsurface. These microorganisms will absorb and scatter part of the incident light, contributing to the total albedo. Then, by simultaneously considering the contributions of water, whitecaps, and chlorophyll, this model presents a more accurate representation of OSA, enabling a clearer differentiation between coastal waters with high phytoplankton concentration and other waterbodies with low biomass, like open-ocean regions.

Water and whitecap albedo at the surface are modeled in the same way as in the Golroodbari model, but here an additional parameter is added to the calculations corresponding to the bioproducts contribution (α_{bp}). In this particular study, only the influence of biological pigment (phytoplankton) is incorporated because its influence is larger compared to other organic substances dissolved in the sea [28]. Furthermore, chlorophyll concentration in seawater has been monitored extensively, and complete datasets are widely available in the literature [22], [29].

This model was tested in two different datasets: LMDZ [30] and ARPEGE-Climat [31], obtaining correlation values of 0.84 and 0.86, respectively. Despite the good correlation result, Seferian's model neglects the backscattering contribution of inorganic compounds. Consequently, as in the case of the Golroodbari's model, **not all relevant parameters are considered in the calculations, leading to a significant limitation in OSA simulations.**

As shown in Table 1.1, the contribution of TSM is neglected in all the existing methods, which becomes a problem when treating turbid waterbodies. Besides, their empirical nature might lead to calculation errors when the models are applied under different environments in which they were formulated, for example, really high chlorophyll concentrations or high whitecaps coverage places.

Item	Symbol	**Golroodbari Model**	**Séférian Model**
Water albedo	α_w	✓	✓
Whitecap albedo	α_{wc}	✓	✓
Organic compounds albedo	α_{bp}	✗	✓
Inorganic compounds albedo	α_{TSM}	✗	✗
Sea roughness	σ	✓	✓

Table 1.1: Variables considered by each model in OSA simulation

1.3. Report Objective and Research Questions

The literature review reveals two primary gaps: (1) unreliable albedo datasets due to their coarse spatial resolution, and (2) empirical models that omit critical factors essential for accurate OSA estimations.

These gaps exist mainly due to the integration of diverse disciplines and the influence of location-specific empirical relationships that fail to generalize across diverse waterbodies.

Addressing such gaps will contribute to a more robust theoretical framework regarding OSA analysis. Therefore, the objective of this thesis is **to develop, validate, and apply a model capable of estimating ocean surface albedo (OSA) in order to assess its impact on the energy yield of offshore floating photovoltaic plants.**

To achieve this objective, the following research questions will be addressed:

1. **How can we modify the in-house developed optical model GenPro4 to model OSA?**
2. **To what extent does the GenPro4-simulated OSA agree with real measurements?**
3. **How does the OSA change under different scenarios, and how do those changes affect the bifacial gain in offshore floating photovoltaic systems?**

2

Application of GenPro4 for Ocean Surface Albedo Simulation

The first research question of the report is addressed in this chapter, aiming to modify the existing GenPro4 model to be suitable for simulating the spectral reflectivity of a water column, including surface and subsurface effects.

As discussed in the previous chapter, there are multiple approaches to model ocean surface albedo (OSA), each varying in complexity. The fundamental distinction among these approaches is the type of variables used for such modeling. Waterbodies are complex and dynamic phenomena. Its inherent changing nature poses significant challenges for a purely physical analysis, as the variables are mostly stochastic and are often interdependent. However, a purely physical model is required as existing approaches rely on empirical relationships that are determined only for a specific region or set of waterbodies. A model that estimates albedo based on inherent physical properties of its constituents can offer a universal view of how to treat this phenomenon, regardless of location or water type constraints.

In this chapter, the physics-based model GenPro4, originally designed to study the optical properties of solar cells, is discussed as an alternative to calculate albedo over wavy surfaces, including the effects present in the water column. First, section 2.1 addresses the approach and simplifications taken to adapt this tool for the simulation of optical phenomena in waterbodies. Then, section 2.2 presents the results obtained when using the GenPro4 model over water columns of varying complexity, analyzing albedo changes across tested cases.

2.1. GenPro4 Modelling

The software GenPro4 [32] is a 1-dimensional simulation tool based on Fresnel equations, which includes ray optics and wave optics to model the optical performance of solar cells. The GenPro4 model simulates a solar cell composed of multiple layers by using, as input, the complex refractive index of each material (n + ik) and the thickness of the different layers or coatings. Based on these parameters, it calculates the reflectivity ($R(\lambda)$), transmission ($T(\lambda)$), and absorption ($A(\lambda)$), along with the photocurrent density generated by each layer.

Several materials can be tested using GenPro4, as long as their refractive indices are known. In this context, a column of water can be discretized into a set of layers, where each one has a different composition (different levels of chlorophyll, inorganic suspended material, among others). This is going to result in a set of layers with different values of n and k, which in turn will define the optical properties of the waterbody: $R(\lambda)$, $A(\lambda)$, $T(\lambda)$. Therefore, an analogy can be established between a solar cell and a waterbody as illustrated in Figure 2.1

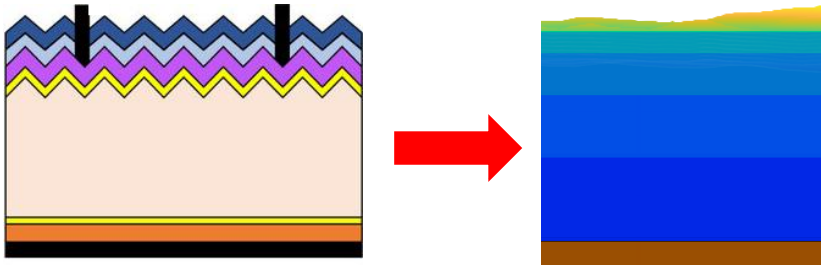

Figure 2.1: Representation of a waterbody as a multilayer system, analogous to the architecture of a solar cell. Bottom layer (brown) corresponding to the seabed, intermediate layers in a scale from blue to blue-green representing the subsurface, and on top an irregular contour layer simulating waves.

Since the objective of this work is the calculation of OSA, the spectral reflectivity is the key parameter of interest. OSA can be calculated from the reflectivity as follows.

$$OSA = \frac{1}{\lambda_2 - \lambda_1} \cdot \int_{\lambda_1}^{\lambda_2} R(\lambda)\, d\lambda \tag{2.1}$$

Considering the aforementioned, GenPro4 offers an alternative to the two models discussed in the literature review. It calculates the same optical parameters, but using a different approach. While Golroodbari and Séférian use parametrized relationships between backscattering and absorption coefficients to calculate OSA, GenPro4 works directly with the n and k of each material, which are intrinsic optical properties, and therefore, they are not affected by empirical parametrization as the other models. As a consequence, the results obtained from GenPro4 could offer a closer look at the actual phenomena.

Nevertheless, before using GenPro4 for simulating the optical properties of the waterbodies, the following obstacles must be addressed.

- GenPro4 is a 1D computational tool; 2D surfaces must be planar and laterally homogeneous in their modeling. This is a problem in the case of whitecaps, as the sea surface is partially covered by foam, leading to a heterogeneous layer that cannot be resolved.
- The subsurface layers of water will have organic and inorganic compounds dissolved in them. This again constitutes a heterogeneous layer, like in the case of whitecaps.

To tackle the first constraint, two simulations are executed with GenPro4 between two limiting cases of the waterbody, foam-free and fully foam-covered. As a result, two different albedos are obtained, one for the foam-free case (α_w), and another for the case when the waterbody is completely covered by foam (α_{wc}). Both variables will be weighted according to Equation 2.2 using the whitecap coverage as the weighting function to obtain the effective mean albedo.

$$OSA = \alpha_w \cdot (1 - f_{wc}) + \alpha_{wc} \cdot f_{wc} \tag{2.2}$$

Regarding the second constraint, organic materials like phytoplankton contribute mostly to light absorption, while inorganic materials, which are mainly mineral particles, have a higher refractive index and low absorption coefficients. Moreover, these particles commonly contribute to light backscattering due to their shape and size.

Absorption coefficients of phytoplankton can be easily integrated with those of seawater to obtain an overall absorption coefficient. Nevertheless, the case of mineral particles is more complex. Backscattering is basically the angular redistribution of radiation. Such direction dependency cannot be simulated in GenPro4 as it is a 1D tool. There is a specific case where the effect of mineral particles can be translated into an effective complex refractive coefficient. In the Rayleigh regime (r < λ, r = particle radii),

the Maxwell-Garnett approach transforms the optical properties of the particle to be included as part of the host water layer. Nevertheless, most mineral particles present in the ocean and most waterbodies have an overall diameter larger than 10 µm; thus, Rayleigh scattering is not an accurate approximation to address the topic.

Due to the lack of an appropriate methodology to assess the optical effect of mineral particles, the zones where the contribution of backscattering is comparable to absorption will not be considered in the study due to the potential errors produced by considering the waterbody as an effective homogeneous medium. For that, **if the contribution of backscattering is less than 20% of the total subsurface contribution to albedo, the assumption of a homogeneous medium is valid**, as it is formulated in Equation 2.3.

$$\frac{b_b}{b_b + a} < 0.2 \implies Homogeneous\ Media \tag{2.3}$$

Appendix A illustrates a map of suitable zones for GenPro4 model applications, considering Equation 2.3.

Regarding the assumptions mentioned above, the overall process carried out by GenPro4 to go from the refractive index of the waterbody to the final albedo value of the water column is depicted in Figure 2.2.

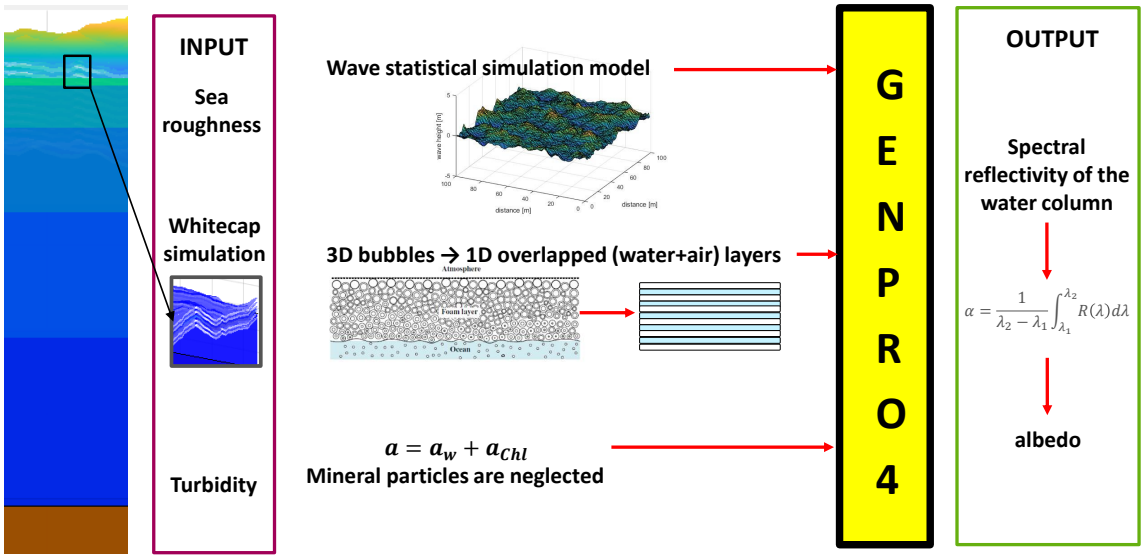

Figure 2.2: Flowchart of the variables used by GenPro4 and the final result given by the tool.

Next, baseline scenarios are modeled to understand the main mechanism of Figure 2.2, and get a deeper understanding of the effect of adding complexity to the waterbody model. Four fundamental cases are treated below, arranged from the simplest to the most complex. The simplest case is simulating a single water layer with a flat surface. The second case introduces wave dynamics to assess the impact of this addition when simulating with GenPro4. In the third case, the effect of whitecaps is incorporated. Finally, the most complex scenario contemplates all previously mentioned variables, along with the discretization of the watercolumn in a set of layers with different chlorophyll concentrations.

2.2. Baseline Scenarios

2.2.1. Flat Sea Surface

The simplest case, consisting of just three layers: an infinite layer of air, an intermediate layer of 27 m of seawater, and below that, an infinite layer of seabed represented by clay, because it is one of the most abundant constituent materials of ocean seabeds [33]. This first configuration is plotted in Figure 2.3, where a seawater layer of 27 meters is placed between an upper infinite air layer and a lower infinite seabed layer.

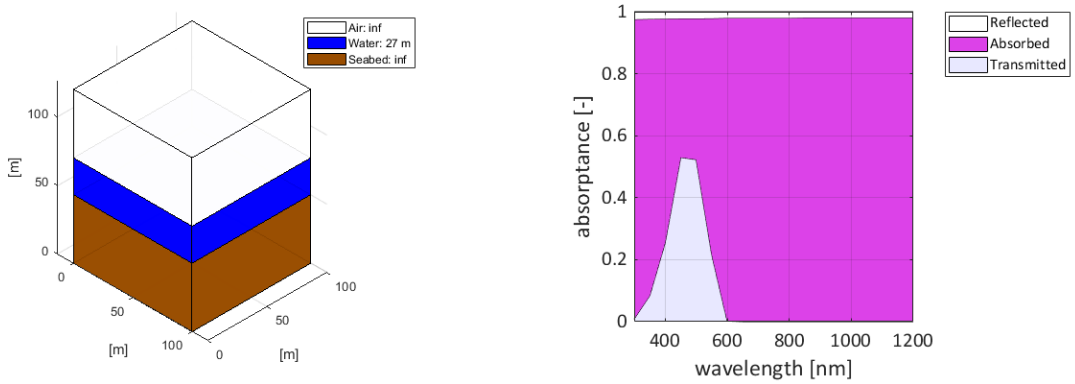

(a) Layers model for flat surface

(b) RAT coefficients

Figure 2.3: Flat Sea surface modelling in GenPro4 using a three layers model (air-water-seabed)

From Figure 2.3, it is observed that the mean reflectivity value (OSA) in this case is 2.2%, which is in the range of the real value when modeling the air-water interface. This value is almost constant throughout all the wavelength spectra (300-1200 nm), which implies that in the flat case, reflection is not heavily affected by wavelength. It can also be observed that water is relatively transparent in the visible range. Figure 2.4 illustrates the values of n and k for seawater. It demonstrates that the extinction coefficient (k) reaches its minimum in the range 300-600 nm, leading to low absorption. Nevertheless, after 600 nm, light is fully absorbed.

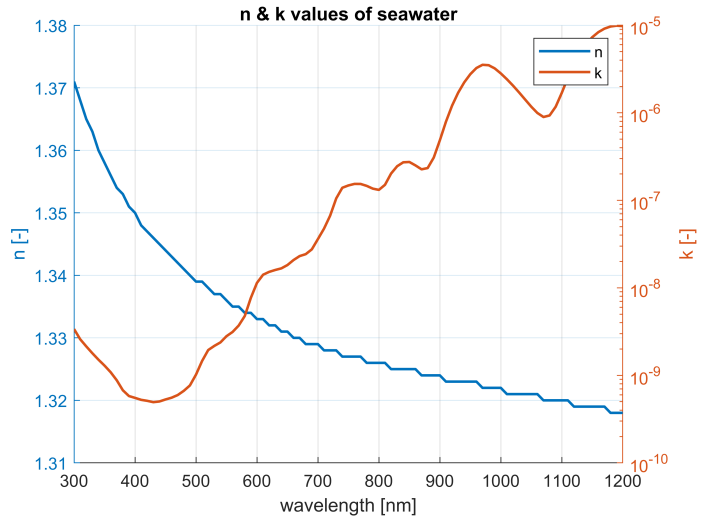

Figure 2.4: Spectral values for n and k coefficients for seawater.

2.2.2. Wavy Sea Surface

In this second scenario, an extra dimension of complexity is added. We incorporated the texture of waves to measure its impact in OSA. A moderate and regular ocean state is considered in this test, defined by a significant wave height H_s = 2 m, and a peak period T_p = 10 s.

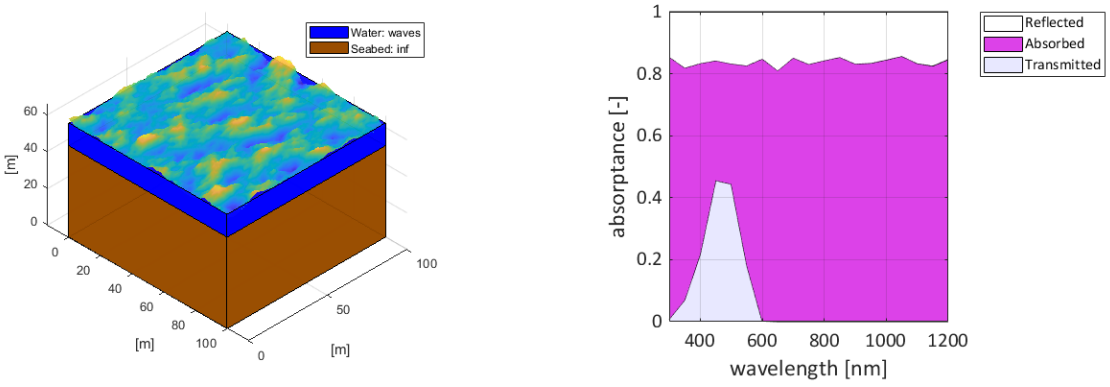

(a) Layers model for wavy surface

(b) RAT coefficients

Figure 2.5: Wavy Sea surface modeling in GenPro4 using a three layers model (air-water-seabed)

Therefore, in this scenario, we have the same three layers (air-water-seabed) with the same dimensions, but the water layer will have a certain roughness due to waves. The effect is already visible by analyzing Figure 2.5b, where an irregular pattern is present throughout the wavelength range and, in fact, the new OSA for this simulation is 16% (8 times higher than the case with a flat surface), which shows the impact of waves on seawater's optical properties. Again, light starts to be fully absorbed from 600 nm, as the extinction coefficient (k) depends only on the type of material and not on geometrical parameters.

From the plot, it can be noted that the albedo of this layer stack has increased by 8 times compared to a flat case. In the context of solar cells, front textures are usually employed to promote light trapping, thereby reducing reflectivity. However, in this case, the reflectivity seems to increase. This is due to the small steepness of waves, which is insufficient to produce internal reflection, but large enough to increase the average incidence angle, which leads to higher Fresnel reflection.

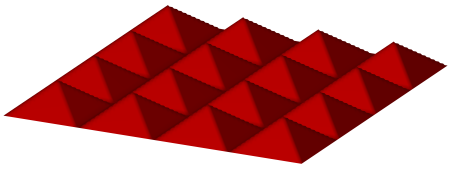

Figure 2.6: textured surface with an area of 50 cm x 50 cm. Pyramids have a side length of 12.5 cm and a height of 5 cm.

Scaling Factor	Pyramid Height (cm)
0	0
0.25	1.25
0.5	2.50
0.6	3.00
0.7	3.50
0.75	3.75
1	5
1.25	6.25
1.5	7.5
1.75	8.75
2	10

Table 2.1: Modified pyramid height when scaling it while keeping the side length constant.

Figure 2.6 illustrates a baseline case of the mentioned above. A textured surface represented by

pyramids is simulated in GenPro4 to assess the variability of albedo when the steepness of the pyramids is tuned. Starting from a default case of 12.5 cm side length and 5 cm height. The height of the pyramid will be scaled according to the factors presented in Table 2.1. The results of the simulations at the different scaling factors are plotted in Figure 2.7.

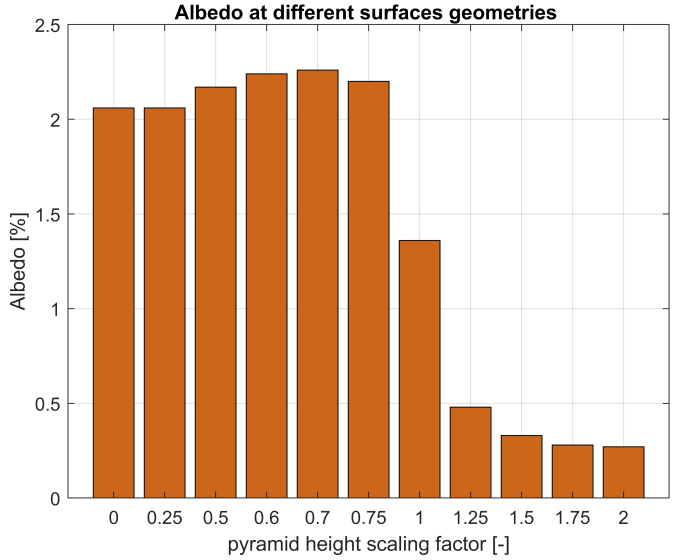

Figure 2.7: Variability of albedo under a pyramidal texture with adjustable steepness. Ranging from flat configurations on the left to highly inclined structures on the right side.

The graph above illustrates the previously discussed trend: increasing surface roughness leads to higher albedo up to a certain threshold. Beyond this point, albedo starts to decrease because internal reflection becomes more significant, producing higher rates of light trapping within the medium. Sea waves typically exhibit roughness values below this threshold, which allows for a maximization of ocean surface albedo (OSA) compared to flat-surface scenarios.

2.2.3. Wavy Sea Surface with Whitecaps

The third case adds the final complexity of simulating foam at the surface resulting from wave breaking. The approach followed in this case is based on [34] that simulates foam as three layers of bubbles (See Figure 2.8) whose characteristics are detailed in Table 2.2.

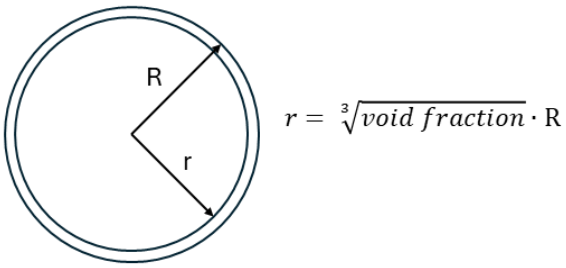

Figure 2.8: Geometrical dimensions of whitecap bubble assuming it to be perfectly spherical

Bubbles are 3D structures, and therefore, cannot be modeled by using GenPro4. Then, each layer of bubbles is transformed into a cluster of overlapped sublayers of air and water as illustrated in Figure 2.9.

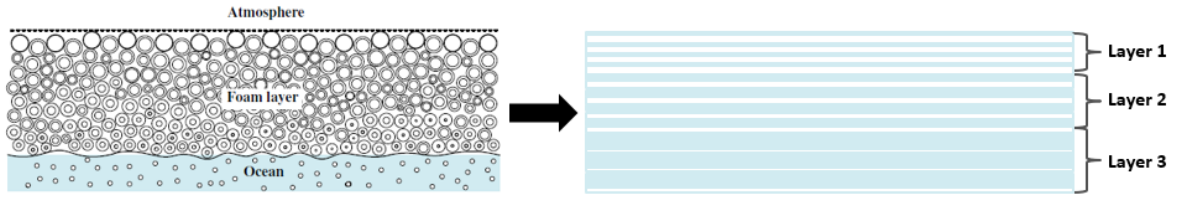

Figure 2.9: Simplification of surface foam discretized as 3 layers of air and water with depth-dependent thickness

For example, in the case of layer 1 (10000 µm thick): Table 2.2 states that 74% of the volume corresponds to bubbles, which are 90% air. This means that air occupies 66.6% of the total layer thickness, roughly 6660 µm out of the total 10000 µm. In the model, each sublayer is assumed to have the thickness of a bubble. To find the diameter, the bubbles are considered perfectly spherical. Based on this assumption, the average bubble diameter in layer 1 is about 948 µm. Finally, by dividing the total air coverage (6660 µm) by the inner diameter of the bubble (948 µm), we get approximately 7 sublayers of air, which are overlapped with 7 sublayers of water of 480 µm thick to complete the total 10000 µm of the whole layer. This procedure is repeated for layers 2 and 3, obtaining a scheme similar to the one depicted in Figure 2.9, whose thickness values of each sublayer are tabulated in the lower part of Table 2.2.

Bubble Model			
Item	**Layer 1**	**Layer 2**	**Layer 3**
Thickness (cm)	1.0	1.0	1.0
Mean Radius (µm)	500	500	500
Bubble void fraction	0.9	0.5	0.1
Bubble volume fraction	0.74	0.74	0.74
GenPro4 Simplification			
Item	**Layer 1**	**Layer 2**	**Layer 3**
Thickness water sublayer (µm)	480	1293	4684
Number of water sublayers	7	5	2
Thickness air sublayer (µm)	948	707	316
Number of air sublayers	7	5	2

Table 2.2: Simplification of foam layers transforming the air bubbles into homogeneous planar layers with the same effective air concentration of the bubbles. Adapted from [34].

A total of 28 sublayers are added on top of the main water layer of 27 m to emulate the effect of whitecaps. The representation of this waterbody column is depicted in Figure 2.10a.

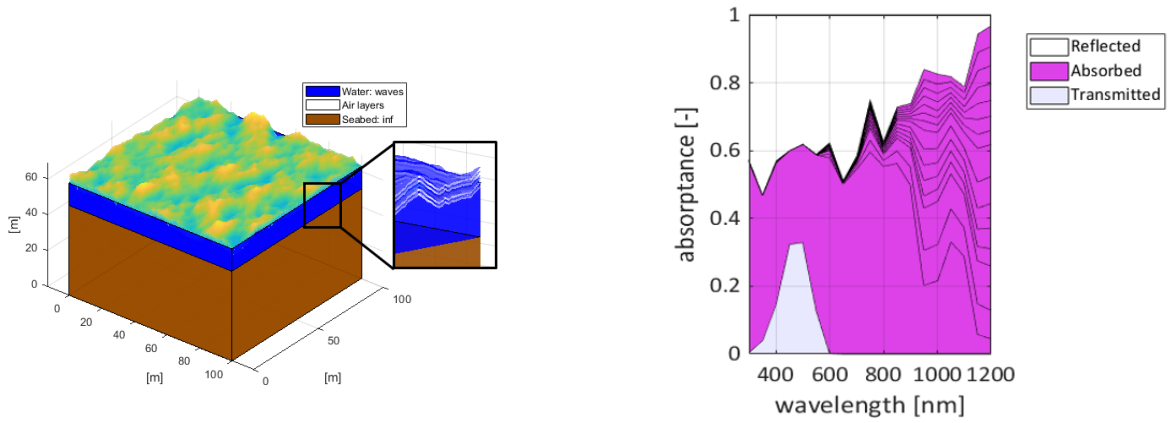

(a) Layers model for wavy surface

(b) RAT coefficients

Figure 2.10: Wavy Sea surface modelling in GenPro4 considering the top surface fully covered by foam

The zoom inset in the picture shows a series of alternating air and water sublayers on top following the same pattern as the wave.

The results of the simulation are depicted in Figure 2.10b, revealing an OSA of 29% (almost double that of the last scenario). Besides, the presence of several peaks across the wavelength range is more pronounced. This is due to the air-water interfaces inside the whitecap structure, which generate enhanced upward reflection, causing sharper peaks at certain wavelengths.

2.2.4. Wavy Sea Surface with Whitecaps and Chlorophyll Profile

The most realistic case to simulate water is adding the contribution of organic and inorganic dissolved material. As it was discussed, one of the simplifications that is taken into account is that only waterbodies with a negligible backscattering coefficient will be considered, which is determined by Equation 2.3. In Appendix A, there is a global map showing all the sea areas out of scope because of the significant backscattering contribution coming from mineral particles. Most coastal zones are deemed unsuitable per this map, whereas offshore regions remain viable due to the low backscattering influences.

Phytoplankton and other organic compounds have a varied and dynamic concentration. It tends to be higher at extreme latitudes, and it changes due to seasonal effects, diminishing in winter and increasing in summer because of higher temperatures. Besides, the concentration is not uniform, but it changes as a function of depth. In [22], a dataset of dissolved material is available to obtain the concentration of chlorophyll and particulate matter that causes backscattering. The concentration of chlorophyll is available for a set of 36 depths [35], which is a valuable set of information, especially in this case.

An effective homogeneous medium considering the effects of pure seawater and chlorophyll results in just adding both absorption coefficients and then extracting the extinction coefficient of the overall value calculated as it is shown in Equation 2.4 and Equation 2.5.

$$a_t(\lambda) = a_w(\lambda) + a_{Chl}(\lambda) \tag{2.4}$$

$$k_t(\lambda) = \frac{a_t(\lambda) \cdot \lambda}{4 \cdot \pi} \tag{2.5}$$

With this, it is possible to obtain the imaginary part of the complex refractive index for the entire range of wavelengths in the effective homogeneous media. To calculate the real part, the Kramers-Kronig relation is used as shown in Equation 2.6.

$$n_t(\omega) = n_w(\omega) + \frac{2}{\pi} P \int_0^{\infty} \frac{\omega' k(\omega')}{\omega'^2 - \omega^2} d\omega'; \qquad \omega = \frac{2 \cdot \pi \cdot c}{\lambda} \tag{2.6}$$

Here, ω represents the angular frequency in rad/s, and P denotes the Cauchy principal value, which handles the singularity in the integral when $\omega' = \omega$. Nevertheless, as the wavelength range treated is a discrete set, the integral becomes a sum, eliminating the need for P.

With these two expressions, it is possible to get the effective complex refractive index of the media regarding the effect of both pure seawater and chlorophyll concentration.

To simulate this waterbody column, the same structure of the last subsection is used, but now, the column is discretized into 36 layers. Each layer's thickness corresponds to depths with known chlorophyll concentration. Then, we get 36 layers with different complex refractive indices that will emulate the optical behavior of the subsurface.

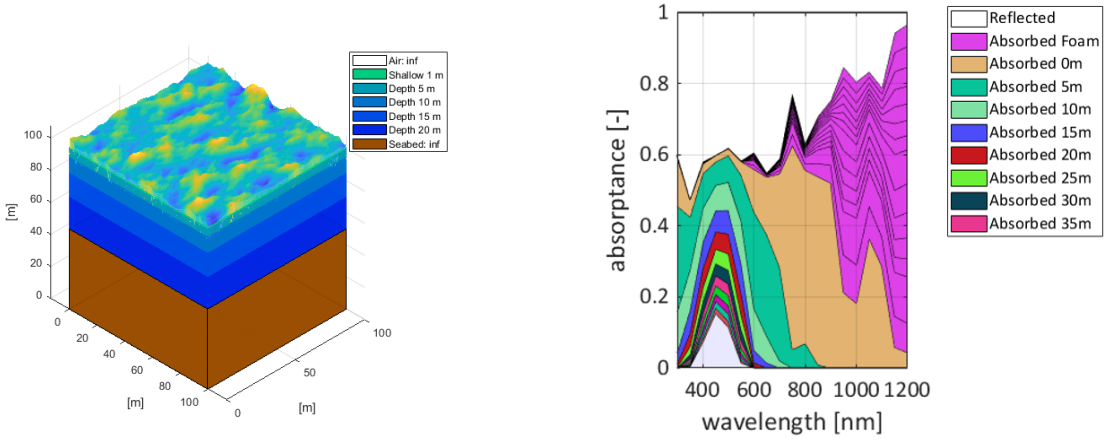

(a) Layers model for wavy surface

(b) RAT coefficients

Figure 2.11: Wavy Sea surface modelling in GenPro4 considering 36 layers with different chlorophyll concentration at certain depths.

As depicted in Figure 2.11a, now the main water layer is reformulated as a cluster of overlapped sublayers. In the picture, the top sublayers are greener as they contain higher chlorophyll concentration, and the deeper it goes, the closer to blue the sublayers are, symbolizing the absence of chlorophyll in them. The results of the optical parameters are plotted in Figure 2.11b, which has a similar pattern compared to the case of only whitecaps, but now the sublayers play a more important role. The portion of light between 300 and 900 nm that was absorbed by pure sea water is now absorbed in the different layers of the chlorophyll-seawater mix. Moreover, the maximum depth reached in this specific case is close to 40 m. Beyond this value, the fraction of light transmitted is below 10% and it is concentrated in the range 400-600 nm where the extinction coefficient of water (k) reaches its minimum (see Figure 2.4).

This full-spectrum simulation is selected for implementation in GenPro4 because it includes the effects of all relevant parameters: waves, whitecaps, and bioproducts present in the subsurface. Then it offers a reliable representation of the dynamic behavior of waterbodies.

2.3. Conclusions of Chapter 2

This chapter aimed to answer the first research question reported in section 1.3: **How can we modify the in-house developed optical model GenPro4 to model OSA?** To do so, several simplifications and assumptions were made, the main ones being: neglecting the contribution of mineral particles and discretizing whitecaps as a cluster of alternating sublayers of water and air with a specific thickness.

Four specific cases were presented in GenPro4 to gain insights about the preliminary importance of each parameter. A flat scenario was tested as a default simulation. Then, a scenario including waves (with a significant wave height H_s = 2m and T_p = 10s was tested to analyze the contribution of this variable, finding that albedo increased by 800%, going from 2% in the flat scenario up to 16% simply by adding the texture of waves on top of the waterbody.

In third place, whitecaps were added to the simulation following the model proposed in [34]. Here, the bubbles were simplified as a set of alternating sublayers of air and water, becoming a 1D input acceptable for GenPro4. In this specific case, under the environmental conditions chosen, the albedo value obtained was almost twice that of the previous case of just waves.

The last scenario tested has the contribution of waves and whitecaps, and additionally, it incorporates the chlorophyll content, by discretizing the waterbody into 36 layers of water with different concentrations of chlorophyll. The results evidenced a similar value of albedo compared to the third case. However, a noticeable difference in the absorption of each layer is obtained, indicating that the contribution of chlorophyll alters the absorption profile more than the spectral reflectivity.

These adaptations proved a high compatibility with GenPro4, successfully integrating all key albedo components in a single model. In conclusion, this validates GenPro4 as a robust tool for simulating albedo in waterbodies.

3

Model Validation of GenPro4

This chapter is linked to the second research question from section 1.3 related to assessing how well GenPro4-simulated reflectivity matches real measurements, to determine the strengths and limitations of the proposed model, as well as identify potential improvements to it.

Ocean surface albedo datasets are scarce, as most of the information available about reflectivity (spectral or albedo) is commonly present for inland locations where interface conditions do not change. Oceanic environments are characterized by highly dynamic interface conditions, which complicate both data acquisition and model validation. Nevertheless, there are some datasets available that, under specific assumptions and with appropriate modifications to the GenPro4 model, can be used to evaluate the numerical results produced against real measured data.

In this chapter, section 3.1 presents a preliminary validation of the modified GenPro4 model against the Golroodbari and Séférian approaches to test the agreement of simulated ocean surface albedo (OSA) under comparable input conditions.

Next, the numerical validation of the proposed model is executed. section 3.2 reviews the available datasets to check the quality and quantity of data that can be extracted from them. In the third section (section 3.3), the proposed model is compared with the measurements obtained in expeditions carried out in the Pacific and Atlantic oceans corresponding to clear waters. This section describes the methodology adopted to perform the validation process, after which the current limitations of the proposed model are analyzed. Subsequently, a set of improvements to the existing model is implemented, and the GenPro4 model is tested again to evaluate the effectiveness of these enhancements. Finally, section 3.4 presents a final validation process for the case of turbid waters, to assess the accuracy of the improved model under specific waterbodies, such as coastal zones.

3.1. Preliminary Validation with Existing Models

The previous chapter explained modifications applied to the simulation process in GenPro4 to model OSA. Nevertheless, it is important to determine its accuracy. For that, it is necessary to compare these results with those of the existing models presented in the literature review.

In this section, the approaches presented in subsection 1.2.3 and subsection 1.2.4 are tested along with the GenPro4 model in two scenarios to get a better understanding of their benefits, limitations, and accuracy-vs-computational cost trade-off. To simulate the three models, the following parameters will remain constant throughout the simulations to ensure that the comparison is executed in similar circumstances.

- Constant wind speed of 18 m/s.
- Calculations made in the range 300-1200 nm.
- Static wave profile based on the parameters H_s = 2m and T_p = 10s.

Therefore, the simulations for the three models to be tested are executed in the following way.

- Golroodbari model: The only required input is the wind speed (set at 18 m/s), because the white-cap coverage and sea roughness are parameters that depend on this variable.
- Séférian model: Again, the wind speed is a required input for this approach. Additionally, the mean chlorophyll concentration (extracted from Copernicus database [36]), along with absorption and backscattering coefficients of water, are required in the model, whose values are found in [37], [27].
- GenPro4 model (Figure 2.2): In this case, along with wind speed, the refractive index of each layer of the water column is required to execute the model. Then, chlorophyll at various depths will be extracted from the Copernicus dataset [35], and by using Equation 2.4, it gives the refractive index of each layer at the waterbody.

With the input parameters defined at each model, simulations can be executed for a selected area to compare their outputs. However, the original Copernicus grid, from which the datasets are obtained, has a spatial resolution of 4 km x 4 km, which is insufficient for accurately modeling Offshore Floating Photovoltaic (OFPV) installations whose typical length scales are inferior to 1 km. Therefore, each 4km x 4km cell is discretized into a grid of 100 x 100 dots, obtaining a separation of 40 meters between dots, which is a reasonable scale to study albedo for OFPV plants. An illustrative example for this discretization is shown in Figure 3.1.

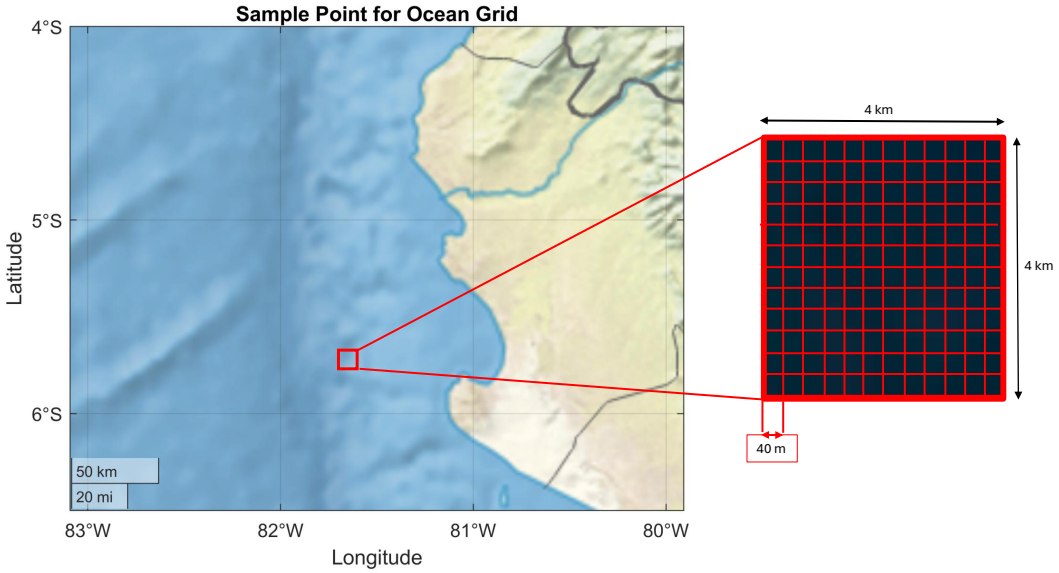

Figure 3.1: Discretization of area to be studied with albedo models.

As the maximum resolution of the dataset is 4 km, for the intermediate points, the data will be obtained via interpolation of the extremes, as properties should not change significantly in the length scale chosen. Furthermore, at each point of the 100 x 100 grid, a specific value of sea height is calculated using the wave spectrum generated by H_s = 2m and T_p = 10s.

By using the methodology described above, two scenario cases are analyzed: North Africa's coast and Peru's coast. The location of these scenarios is depicted in Figure 3.2.

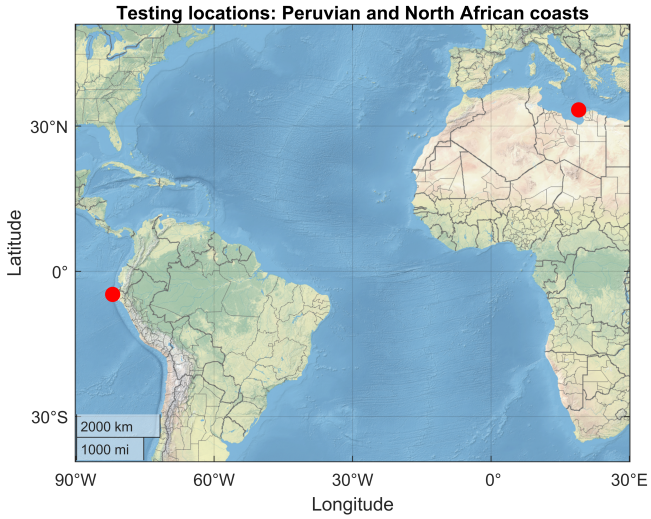

Figure 3.2: Location selected for preliminary validation: Peruvian coast with high Chl concentration (5°S - 82°W) and North African coast with low Chl concentration (33°N - 19°E).

The portion of the sea located in the coordinates 33°N - 19°E corresponds to the coastal part of the Mediterranean Sea belonging to North Africa. This area is characterized by a surface temperature range between 15 and 26°C, coastal waves in the range 0.3-1.3 m, and a relatively low chlorophyll concentration with a mean value of 0.30 mg/m^3 near the coast and 0.11 mg/m^3 in open waters [38, 39]. The above makes this area an ideal representation for a clear and low chlorophyll-level sample.

In contrast, the eastern coast of South America is characterized by cold and nutrient-replete waters. This drives a high biological productivity which translates into big concentrations of chlorophyll in the order of 2 mg/m^3 [40]. In terms of oceanographic characterization, the temperature range of the coastal waters is 16-25°C with typical wave elevations between 1-3 m.Such characterization converts this area into a reliable case to study the contribution of microorganism pigmentation, avoiding the risk of analysis contamination because of the influence of additional parameters.

The chlorophyll concentration levels in both locations across the year are depicted in Figure 3.3.

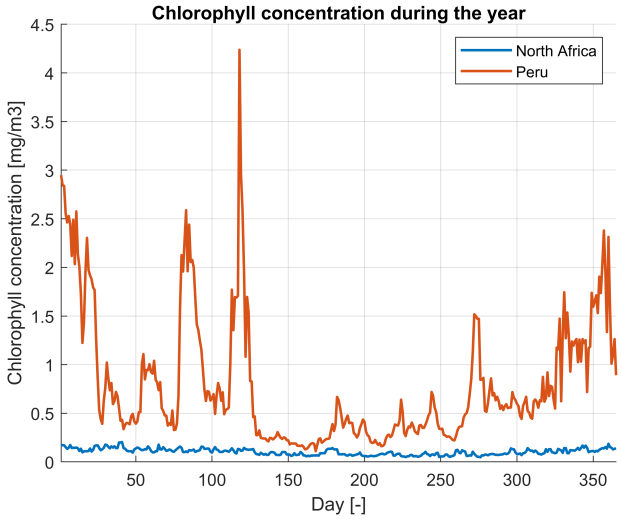

Figure 3.3: Daily chlorophyll concentration during the year 2021 at North African and Peruvian coasts.

The coast of North Africa exhibits an average concentration of approximately 0.2 mg/m^3 with no signif-

icant changes throughout the year. In contrast, for the case of the Peruvian coast, chlorophyll concentration is quite volatile, reaching values as high as 4 mg/m^3.

When simulating OSA with the Séférian and Golroodbari models at both study locations, a full-year timespan was selected, spanning from 01-01-2021 to 31-12-2021 on a daily basis, obtaining 365 albedo calculations. These daily outputs were subsequently averaged to derive the mean annual OSA, along with its associated spectral reflectivity distribution. For the GenPro4 simulation, to save computational costs, the annual mean chlorophyll concentration was used as input, enabling a single simulation run; this produced equivalent outputs of mean OSA and spectral reflectivity.

The results of the simulation at both locations are shown in Figure 3.4, where the spectral reflectivity obtained by each model is plotted as a function of wavelength.

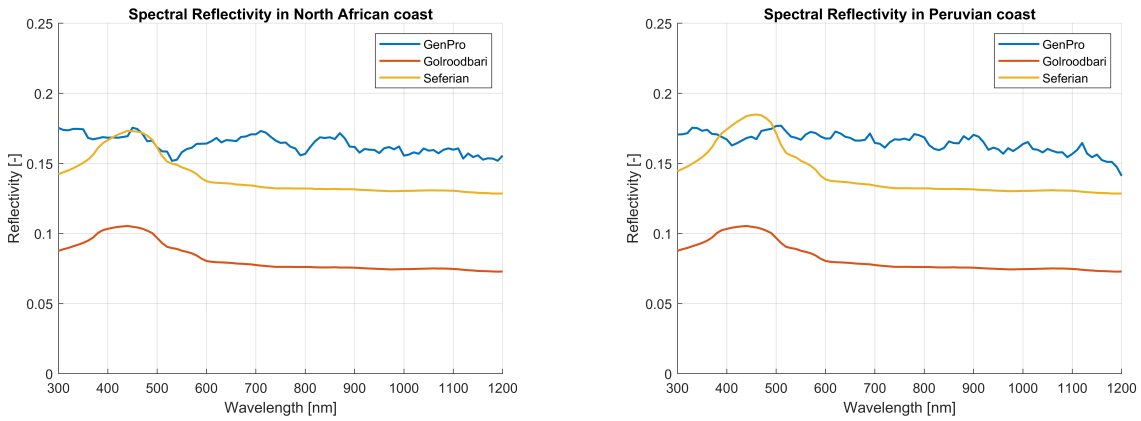

(a) Spectral reflectivity in the North African coast.

(b) Spectral reflectivity in the Peruvian coast

Figure 3.4: Spectral reflectivity in (a) North Africa's coast and (b) Peru's coast obtained when simulating the three models discussed: Golroodbari, Séférian, and GenPro4.

As observed, among all simulations, the results of GenPro4 are the only ones where peaks and valleys are obtained. The main reason for this effect is found when analyzing the sea profile. Golroodbari and Séférian's are analytical models. They take as input the average roughness of the sea and the zenith angle to calculate an empirical coefficient to simulate the effect of waves over OSA. Nevertheless, the GenPro4 model uses ray tracing when calculating, and it takes into account the real geometry of the facet, which in turn could lead to the observed peaks, as different wavelengths have different responses to a certain and static wave facet.

When comparing Figure 3.4b and Figure 3.4a, it is possible to appreciate that both curves are almost identical throughout the entire spectrum. The cases of North Africa and Perú were chosen because both locations share similar environmental conditions except for chlorophyll concentration, as it is depicted in Figure 3.3. Despite these differences, both plots present similar results which indicates that the difference in chlorophyll concentration in these two locations is too low to produce significant changes in the spectral reflectivity.

GenPro4 exhibits a flatter spectral profile compared to the Séférian and Golroodbari models, which present a peak around 450 nm. Despite the spectral trend is not identical between the cases, GenPro4 remains suitable for OFPV albedo studies because its results align closely to Séférian's numerical values, obtaining OSA values of 0.143 (Séférian) versus 0.162 (GenPro4) for the North African coast and 0.144 (Séférian) versus 0.161 (GenPro4) for the Peruvian coast.

This match between GenPro4 and the Séférian model validates our model for practical applications. However, the GenPro4 model's true accuracy must be validated against in situ albedo (or spectral reflectivity) measurements. Therefore, in the following sections, the available albedo datasets are presented, and the numerical validation of GenPro4 with these datasets is executed.

3.2. Available Data for Ocean Surface Albedo

The primary output generated by GenPro4 is a matrix of size $m \times n$, where m is the number of wavelengths considered during the simulations and n is the number of interfaces defined in the water column within the model. Therefore, in this matrix, it is possible to obtain the spectral reflectivity of the entire stack, the spectral absorptance of each layer, and, in the bottom row, the spectral transmittance in case that residual radiation reaches the base of the water column.

Three main global OSA datasets capture this parameter worldwide [41]. Nevertheless, these datasets are characterized by coarse spatial resolution and low sampling frequency; consequently, many latitudes and longitudes are not covered. A detailed description of these datasets, together with their limitations, is provided in Appendix B. Regarding this contraints, global OSA datasets are not suitable for use as a validation reference.

Consequently, rather than relying on global products, this study adopts more localized datasets that cover a smaller region of the world but provide detailed in situ measurements, thereby establishing a basis for robust model validation.

In the present work, two main datasets will be used to validate the GenPro4 model. One of them gathers measurements for clear waterbodies, while the other one contains measurements for turbid waters, collected in environments such as estuaries and rivers where suspended particle concentrations are significantly higher. Both datasets are described below.

3.2.1. Dataset for clear water

The Biogeochemistry and Optics South Pacific Experiment (BIOSOPE expedition) [42], hereafter referred to as 'dataset 1', was an extensive oceanographic campaign that covered a route of approximately 8000 km. This expedition encompassed a significant portion of the central and southern part of the Pacific and Atlantic oceans, as illustrated in Figure 3.5.

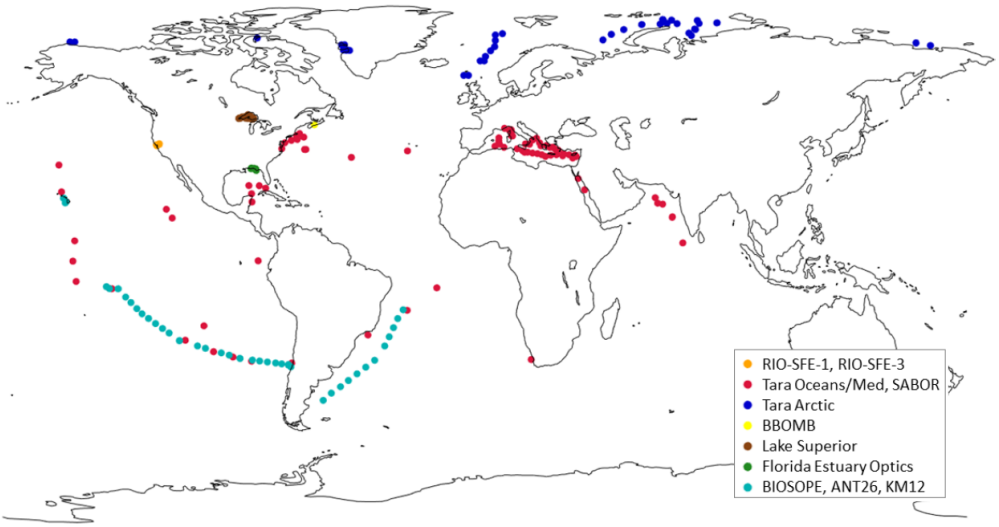

Figure 3.5: Coordinates of places chosen for different scientific expeditions. BIOSOPE cruise marked with the light blue dots. Extracted from [42].

This dataset offers a total of 16 sample points with a set of measured parameters, as it is shown in Table 3.1

Expedition	n° samples	a_{CDOM}	a_{NAP}	a_p	a_{ph}	b_{bp}	$R(\lambda)$
BIOSOPE	16	✓	✓	✓	✓	✓	✓

Table 3.1: Variables measured by each expedition

. This dataset represents an ideal basis for the present analysis, as it includes the spectral reflectivity ($R(\lambda)$) and the key optical components that define the subsurface radiative dynamics: absorption coefficient (a) and backscattering coefficient (b_b). The methodology used to acquire these data and the spectral range covered by each variable is described in detail in Appendix B.

3.2.2. Dataset for turbid waters

The final dataset to be discussed is Remote Sensing of Turbid Waters in the Short Wave Infrared project (Sea SWIR expedition) [43], hereafter referred to as 'dataset 2'. This dataset contains a total of 5 data points, for which spectral reflectivity data of turbid estuarine waters were measured on different days. The measurements were conducted in Gironde (France), La Plata (Argentina), and Scheldt (Belgium). These locations were chosen because of their elevated turbidity levels, ranging from 48 to 1400g/m^3. This wide range of total suspended matter (TSM) provides a valuable basis to analyze the role of this variable on the overall calculation of spectral reflectivity in waterbodies.

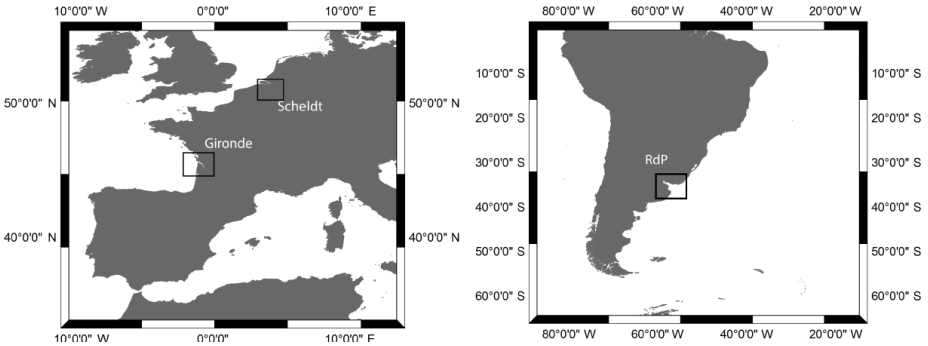

Figure 3.6: Geographic zones where measurements were taken in the SeaSWIR expedition. Extracted from [43]

This dataset offers the spectral reflectivity along with the concentration of mineral particles in the waterbody. Therefore, due to the lack of absorption and backscattering coefficients in the dataset, these must be collected separately from the Copernicus website [22] to add them into the dataset prior to analysis. Again, the details of the methodology to extract the data can be found in Appendix B.

Taken together, the two datasets (representative of clear and turbid waters) constitute a robust framework to test the accuracy of the GenPro4 model developed in the previous chapter. Such validations are presented in the following section.

3.3. Comparison with the dataset for clear waters

3.3.1. Methodology and Results

Before starting with the validation step, it is important to consider the limitations of the current dataset. The primary constraint is that the reflectivity values of the dataset are not equivalent to those generated by GenPro4.

When analyzing sun radiation, there is a downwelling irradiance ($E_d(\lambda)$) corresponding to the sun rays coming from the sun in the direction to the Earth, as illustrated in Figure 3.7. At the same time, upwelling irradiance ($E_u(\lambda)$) corresponds to the radiation that is redirected upwards after interacting with the environment. In the case of waterbodies specifically, E_u can be decomposed into two main components: interface irradiance ($E_{interface}(\lambda)$) which arises from the radiation reflected in the air-water interface at the sea, and water-leaving irradiance ($E_{wl}(\lambda)$), which represents the radiation redirected upwards once it interacts with substances present in the bulk water column, like organic compounds or mineral particles (See Figure 3.7).

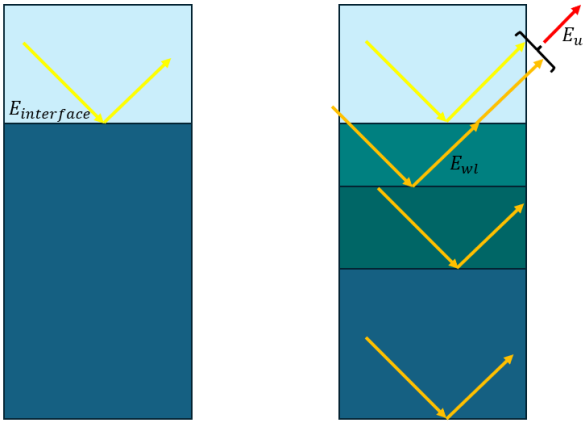

Figure 3.7: Decomposition of upwelling irradiance ($E_u(\lambda)$) into its main components: interface irradiance ($E_{interface}(\lambda)$) and water-leaving irradiance ($E_{wl}(\lambda)$).

GenPro4 analyzes the overall optical interaction, which is reflection at the interface plus further reflections in the bulk of the waterbody. The spectral reflectivity of this model is given by Equation 3.1.

$$R(\lambda) = \frac{E_{interface}(\lambda) + E_{wl}(\lambda)}{E_d(\lambda)} = \frac{E_u(\lambda)}{E_d(\lambda)} \tag{3.1}$$

In contrast, the data of spectral reflectivity given by dataset 1 only considers the upwelling water-leaving irradiance, neglecting the contribution of the air-water interface. Then, the reflectivity of dataset 1 is defined as:

$$R(\lambda) = \frac{E_{wl}(\lambda)}{E_d(\lambda)} \tag{3.2}$$

This represents a key constraint, as the model and validation dataset present different reflectivity outputs. To match the format of dataset 1, two separate analyses are performed using GenPro4.

The first simulation contemplates the complete scenario, including all substances present in the bulk of the waterbody, as illustrated in the right column of Figure 3.7. This simulation gives the result of Equation 3.1. The second simulation, depicted in the left column of Figure 3.7, only considers a layer of air and a layer of seawater. Then, as there are no substances present in the bulk of the waterbody (it is a column of pure seawater), no internal reflection will occur, and consequently, there will be no water-leaving irradiance. Therefore, the result of this second simulation represents only the optical phenomena occurring at the air-water interface.

By subtracting the result of the second simulation from that of the first, the result is the one given in Equation 3.3. This result corresponds directly to the variable defined in Equation 3.2 for the spectral reflectivity of the dataset.

$$R(\lambda) = R_{overall}(\lambda) - R_{deep\ water}(\lambda) = \frac{E_u(\lambda) - E_{interface}(\lambda)}{E_d(\lambda)} = \frac{E_{wl}(\lambda)}{E_d(\lambda)} \tag{3.3}$$

For simplicity, and due to the lack of information regarding the wave conditions at the measurement sites, a flat water surface is assumed (no waves). This assumption is justified by the size of the measurement equipment: buoys used to register irradiance typically measure only a few tens of centimeters, meaning that the effect of sea roughness is negligible. Furthermore, because the reflectivity at the air-water interface is excluded from the comparison, the simplification of a flat surface is appropriate for the validation.

As shown in Table 3.1, along with phytoplankton, other organic materials like coloured dissolved organic matter (CDOM) and non-algal particles (NAP) are included. The absorption coefficients of these substances, combined with those of mineral particles, are available as measured data from the expedition's data points. The backscattering coefficient is not included because, as discussed in the previous chapter, the effect of backscattering is not compatible with the processing of GenPro4, which operates as a 1D model. Additionally, it is necessary to include the effect of water in the absorption coefficient calculation, which can be found at [27].

These five absorption coefficients are added up, and an overall value is obtained, from which the attenuation coefficient of the layer can be calculated by using Equation 3.4.

$$a_t(\lambda) = a_w + a_{CDOM}(\lambda) + a_{NAP}(\lambda) + a_p(\lambda) + a_{ph}(\lambda) \rightarrow k_t(\lambda) = \frac{a_t(\lambda) \cdot \lambda}{4 \cdot \pi} \tag{3.4}$$

Using this approach, the equivalent imaginary part of the complex refractive index ($k(\lambda)$) can be determined, while the real part ($n(\lambda)$) will be calculated using the Kramers-Kronig relations (Equation 2.6). It is important to note that the real part of the refractive index is expected to remain unchanged relative to tabulated values of seawater, since the concentrations of chlorophyll and minerals are not high enough to significantly affect this variable. Following this procedure, both $n(\lambda)$ and $k(\lambda)$ are obtained for the whole spectrum, and the waterbody is fully defined to become an input in GenPro4 simulation, enabling the model to be run.

A total of 14 points were chosen from dataset 1 as they are distributed in an equidistant way, representing an adequate sample for comparison purposes. The geographic coordinates chosen for the validation are plotted in Figure 3.8, which illustrates that they are located in open-ocean areas, meaning that such points correspond to clear water conditions.

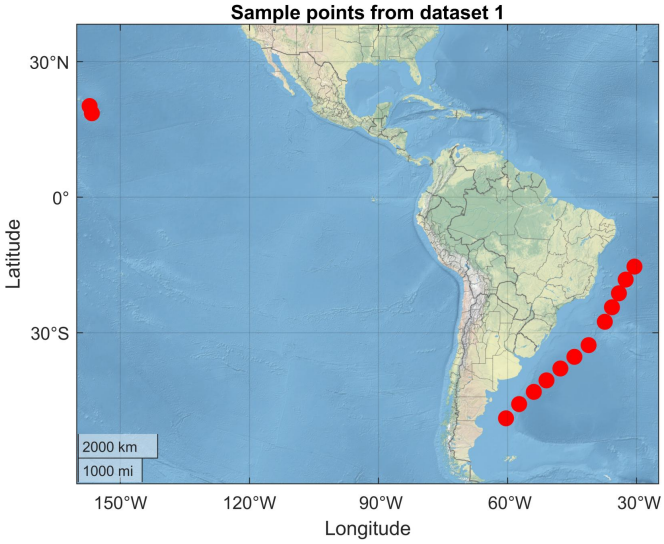

Latitude [°]	Longitude [°]
-45.59	-60.35
-43.23	-57.30
-41.13	-53.88
-39.09	-50.94
-36.92	-47.71
-34.72	-44.45
-32.46	-41.14
-27.77	-37.38
-24.75	-35.72
-21.77	-34.10
-18.79	-32.53
-15.91	-30.49
20.69	-157.15
19.13	-156.62

Figure 3.8: Sample data points taken from dataset 1 for numerical validation GenPro4 model in clear waters.

All the variables presented in Table 3.1 are measured in a spectral mode at each coordinate point of Figure 3.8. Additionally, all the absorption coefficients are measured at a depth of 3 m. Then, for GenPro4 calculations, the water column will be discretized into three main layers: A semi-infinite layer of air, a 3 m layer of water containing organic compounds whose overall absorption coefficient is given by Equation 3.4, and a semi-infinite layer of pure seawater whose absorption coefficient is given exclusively by water (no addition of organic compounds). The schematic representation of this configuration is provided in Figure 3.9.

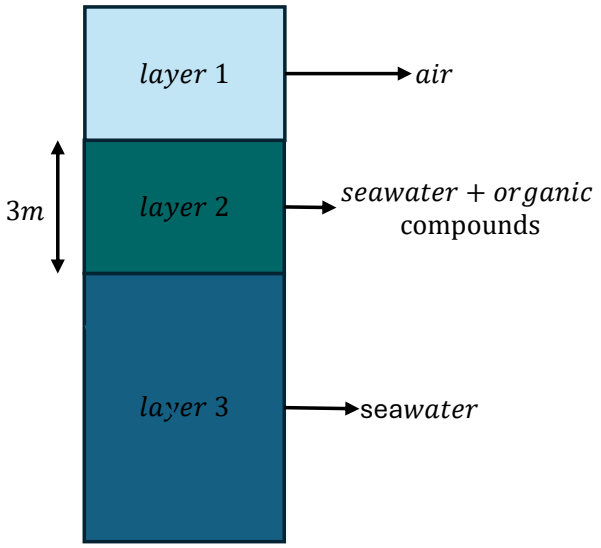

Figure 3.9: Representation of water column to be simulated in GenPro4

As a mode of example, for the first data point (45.59°S - 60.35°W), Table 3.2 shows the absorption coefficients measured in this cruise at intervals of 100nm (the real dataset contains the data from 350 to 900 nm at a resolution of 10 nm). The values for the coefficients of water are, again, extracted from literature [27].

	400	500	600	700	800	900
a_w	0.0173	0.0256	0.2388	0.6481	2.068	6.776
a_p	0.0558	0.0427	0.0113	0.0050	0.0021	0
a_{ph}	0.0418	0.0343	0.0095	0.0015	0.0004	0
a_{NAP}	0.0139	0.0083	0.0054	0.0035	0.0026	0
a_{CDOM}	0.0799	0.0157	0.0030	0.0060	0.0001	0

Table 3.2: Spectral coefficients at selected wavelengths for waterbody whose optical properties are measured at the coordinates 45.91°S - 60.35°W

Using the spectral data summarized in Table 3.2, the GenPro4 model is executed, and the resulting outputs are then compared with the values of the dataset. The comparison results of both cases are presented in the plot below.

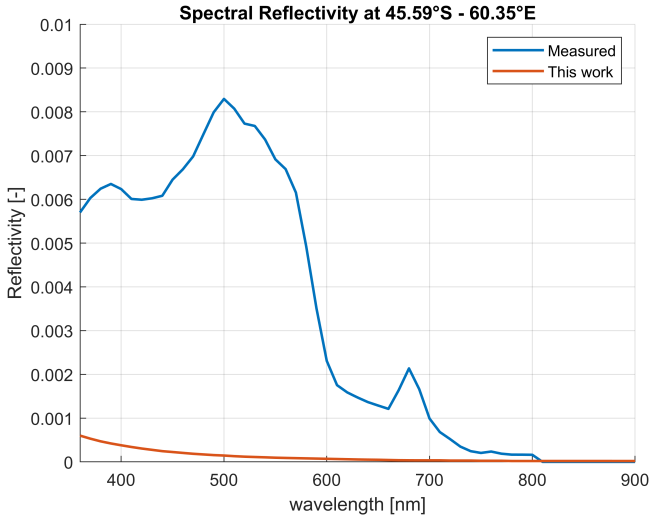

Figure 3.10: Comparison of spectral reflectivity measured as data and simulation using GenPro4

A clear discrepancy is observed between the two curves. The measured data show considerable reflectivity values in the short-wavelength range of the spectrum and then an exponential decay until reaching zero at approximately 750 nm. In contrast, the spectral reflectivity simulated by GenPro4 is practically flat, meaning that the contribution of upwelling irradiance coming from the subsurface of the waterbody is practically negligible. It is important to clarify that the GenPro4 simulation is carried out as the difference between the complete model, including all defined layers, and the simple model of just a semi-infinite column of water as treated in Figure 3.7

The dominant optical process simulated in GenPro4 is interface reflectivity calculated via Fresnel equations; consequently, the refractive index of each layer plays an important role in the overall model output. The real and imaginary parts of each layer are plotted in Figure 3.11.

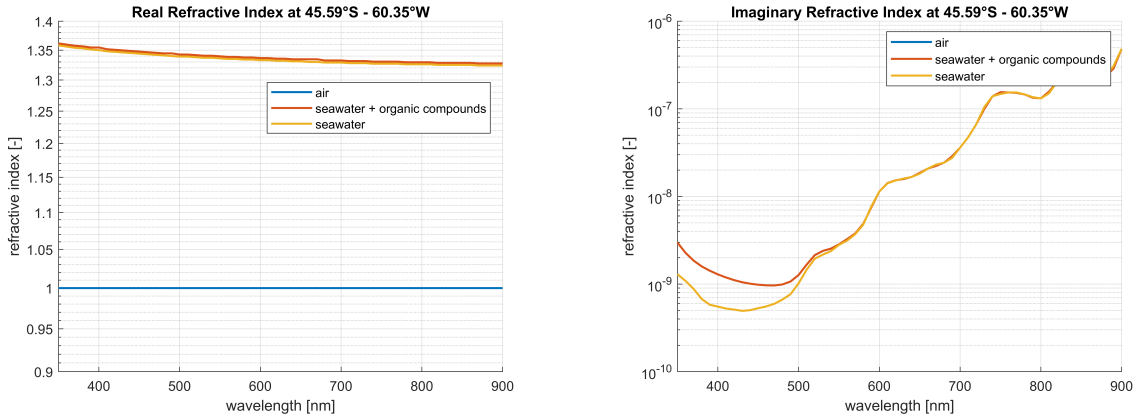

(a) Spectrum of real refractive index $n(\lambda)$

(b) Spectrum of imaginary refractive index $k(\lambda)$

Figure 3.11: Spectral representation of the complex refractive index ($n(\lambda) + ik(\lambda)$) in the three layers of the water column simulated.

In the left graph, the real part of the refractive index $n(\lambda)$ is plotted for the three layers of Figure 3.9. There is a noticeable difference between the layers of air and seawater, which leads to non-zero reflectivity values according to the Fresnel equations. Nevertheless, for the bulk of the waterbody, this is between the layers of seawater and seawater + organic compounds, the real values of the refractive index are practically the same, resulting in negligible water-leaving irradiance.

In the right graph, the extinction coefficient $k(\lambda)$ is depicted. This coefficient is mainly associated with absorption. Besides, as $k(\lambda)$ is several orders of magnitude lower than $n(\lambda)$, the complex refractive index is dominated mainly by its real part, making $n(\lambda)$ the primary parameter in the Fresnel equations. Furthermore, beyond 600 nm, the curves of seawater and seawater + organic compounds merge, indicating that the absorption phenomenon in the water column starts to be fully dominated by the intrinsic absorption coefficient of water.

This behaviour is explained by the nature of the waterbody and the modelling approach employed. Organic components are present only in small concentrations in seawaters, and they are practically dissolved in it, so their primary optical effect is to add an absorption component to the bulk medium rather than behaving as a high-contrast scatterer.

Since chlorophyll and the other compounds considered in the case studied do not contribute significantly to the reflectivity in the waterbody, there must be another component responsible for the water-leaving irradiance in the short-wavelength region of the spectrum (see Figure 3.10). As discussed in section 2.1, one of the main assumptions considered is to ignore the contribution of mineral particles as they produce reflection mainly via backscattering, which can not be included in GenPro4. Nevertheless, its influence can be significant in waterbody albedo analysis, requiring its incorporation in the overall assessment.

The following subsection presents an approach for including the backscattering effect of mineral particles, along with the strategy for integrating these into GenPro4 outputs.

3.3.2. Limitations of the current model and further improvement

As it was shown in the previous subsection, considering the contribution of particles could be essential to achieve an accurate modelling of the bulk reflectivity given by water-leaving irradiance. Because mineral particles are not dissolved, but maintain their structure in the seawater, they scatter light due to their size and refractive index different from that of water. Backscattering is the main contributor to water leaving irradiance, and therefore, it is important to include its contribution in the subsurface dynamics. This phenomenon is an angular redistribution of incoming light that cannot be represented in GenPro4 (due to 1D limitations), and, consequently, a different approach is needed to add its effect to albedo calculations. In waterbodies, there are two main contributors of backscattering: **water** and **mineral particles**.

In the first case, the values of water scattering coefficients are tabulated in existing literature [37]. As water particles are highly symmetrical, they disperse light evenly in all directions. Therefore, to get the backscattering coefficient, it only remains to multiply the overall scattering coefficient b_w by 0.5, as half of all dispersed radiation will be directed upwards. According to this, the backscattering coefficient of water b_{bw} is obtained as follows.

$$b_{bw}(\lambda) = 0.5 \cdot b_w(\lambda) \tag{3.5}$$

The case of particles in seawaters is considerably more complex. In the sea, we find particles of different sizes, shapes, and compositions. These three factors are relevant for the calculation of the backscattering coefficient, and therefore, it is not simple to establish a universal formula to calculate this coefficient for all marine particles. Instead, these values are obtained experimentally via measurements in different cruises or via satellite, just like the case of chlorophyll concentration.

In such datasets, the backscattering coefficient is usually reported at a specific reference wavelength, obtaining a single value for this parameter. Nevertheless, the spectra of this variable are modeled using an exponential decay function, as shown in Equation 3.6, where the exponent γ depends on the specific characteristics of the waterbody, but a value of 1 is often used for simplicity [44], and is therefore adopted in this work.

$$b_{bp}(\lambda) = (\frac{\lambda_0}{\lambda})^{\gamma} \cdot b_{bp}(\lambda_0) \tag{3.6}$$

In Equation 3.6, λ_0 is the wavelength at which the parameter is measured, and λ is an arbitrary wavelength at which the value of backscattering is to be estimated.

The overall backscattering coefficient within the waterbody corresponds to the addition of those two variables. Since this parameter is also an inherent optical property (IOP), the contribution from different components can be added up linearly.

$$b_{bt}(\lambda) = b_{bw}(\lambda) + b_{bp}(\lambda) \tag{3.7}$$

With the overall backscattering coefficient already defined, the spectral reflectivity produced by this parameter in a bulk and homogeneous medium is defined according to Equation 3.8 [45].

$$R_{bulk}(\lambda) = \frac{f}{Q} \cdot \frac{b_{bt}(\lambda)}{b_{bt}(\lambda) + a_t(\lambda)} \tag{3.8}$$

In Equation 3.8, the ratio $\frac{f}{Q}$ represents the backscattering efficiency, which is a relation between forward and backward scattering. In the case of oceans and most of the waterbodies, a value of 0.11 is widely accepted [46], and is therefore adopted in this work. Then, the reflectivity produced by the particles present in the waterbody is completely defined by the absorption and backscattering coefficients present in the water column.

This additional approach to calculate the bulk reflectivity of the subsurface is added separately from the GenPro4 model, resulting in a new model version that accounts for both optical mechanisms. Consequently, the overall spectral reflectivity will be expressed by the sum of the air-sea interface reflectivity ($R_{interface}(\lambda)$) given by the GenPro4 simulation, and the subsurface reflectivity ($R_{bulk}(\lambda)$) computed using Equation 3.8.

$$R_{sea}(\lambda) = R_{interface}(\lambda) + R_{bulk}(\lambda) \tag{3.9}$$

This new model obtained in Equation 3.9 will be used to re-evaluate dataset 1, and verify the accuracy of the improvement applied.

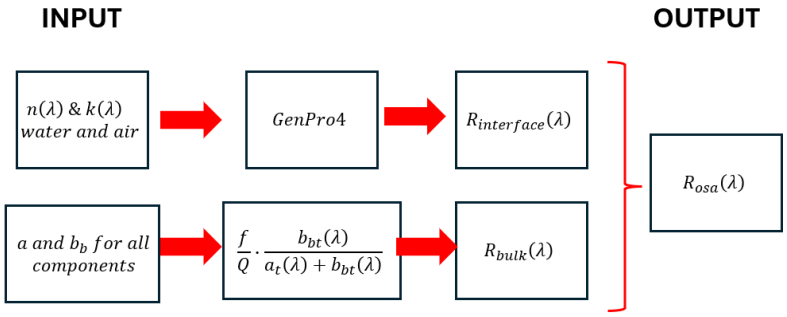

Figure 3.12: Flowchart of improved GenPro4 model

3.3.3. Validation of the improved GenPro4 model

Dataset 1 includes data for both absorption and backscattering coefficient of substances present in the bulk of the water column, as summarized in Table 3.2. In the specific case of the backscattering coefficient of particles (b_{bp}), this parameter is only measured for specific wavelengths during the expedition. Therefore, Equation 3.6 is used to obtain the values for the rest of the spectrum, considering the following.

- $\gamma = 1$ because it is the reference value for open waters with low turbidity, such as oceans [44].

- b_{b0} will be chosen at $\lambda = 639$nm, because typical values to originate the spectral version of backscattering rely on the range 550-650nm, to avoid strong absorption in the blue range or low signal in infrared spectra, and 639nm is the closest value in the dataset to this range [44].

Following the flowchart depicted in Figure 3.12, the calculation process is divided into two main steps.

- Interface reflectivity carried out by GenPro4 assuming only a top semi-infinite layer of air and a bottom semi-infinite layer of water as depicted on the left side of Figure 3.7. A flat surface is assumed, and the refractive index $n(\lambda)$ and $k(\lambda)$ of water and air are extracted from literature [27].
- Bulk reflectivity representing the dynamics of the waterbody subsurface. In this approach, all spectral values provided in dataset 1, together with the corresponding coefficients of pure water, are summed to obtain a total absorption and backscattering coefficient as shown in Table 3.3

	400	500	600	700	800	900
a_w	0.0173	0.0256	0.2388	0.6481	2.068	6.7776
a_p	0.0558	0.0427	0.0113	0.0050	0.0021	0
a_{ph}	0.0418	0.0343	0.0095	0.0015	0.0004	0
a_{NAP}	0.0139	0.0083	0.0054	0.0035	0.0026	0
a_{CDOM}	0.0799	0.0157	0.0030	0.0060	0.0001	0
a_t	0.2087	0.1266	0.2679	0.6641	2.0732	6.7776
b_{bp}	0.0065	0.0036	0.0025	0.0019	0.0015	0.0014
b_{bw}	0.0037	0.0014	0.0007	0.0003	0.0002	0.0001
b_{bt}	0.0102	0.0050	0.0032	0.0022	0.0017	0.0015

Table 3.3: Spectral coefficients at selected wavelengths for waterbody whose optical properties are measured at the coordinates 45.91°S - 60.35°W, including backscattering contributions

These coefficients will be introduced in Equation 3.8 to get the spectral bulk reflectivity (considering $\frac{f}{Q} = 0.11$)

Since dataset 1 only presents values for water-leaving irradiance, only the bulk reflectivity given by the physical approach will be tested in this case. The results of such simulations are depicted in Figure 3.13, showing the spectral reflectivity for the 14 data points chosen with the root mean square errors (RMSE) of each case.

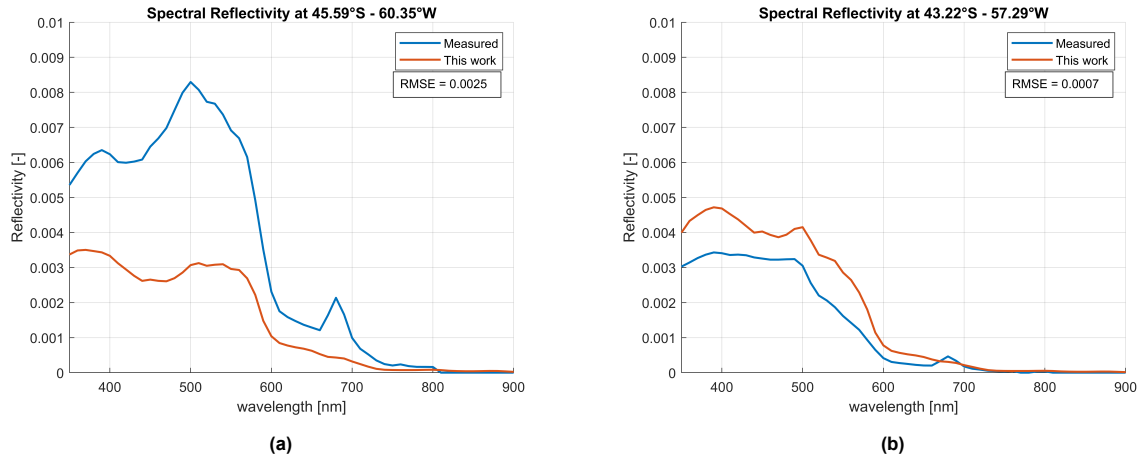

(a) (b)

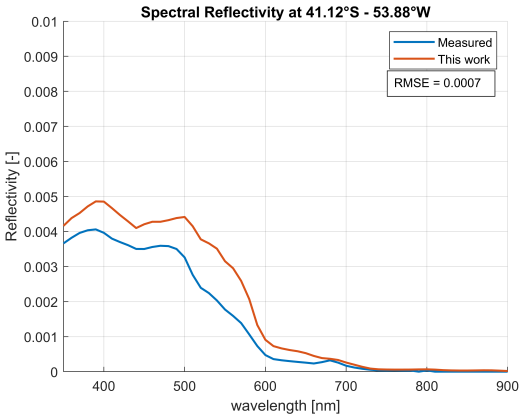
Spectral Reflectivity at 41.12°S - 53.88°W
Measured
This work
RMSE = 0.0007
Reflectivity [-]
wavelength [nm]

(c)

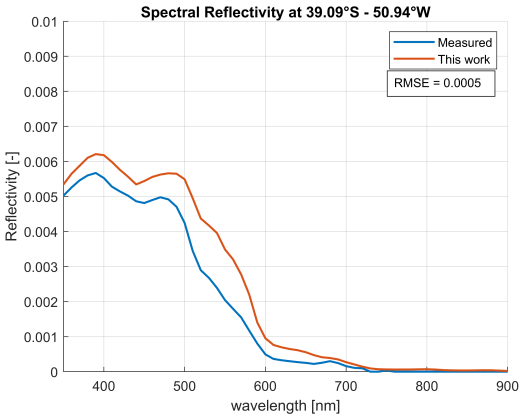
Spectral Reflectivity at 39.09°S - 50.94°W
Measured
This work
RMSE = 0.0005
Reflectivity [-]
wavelength [nm]

(d)

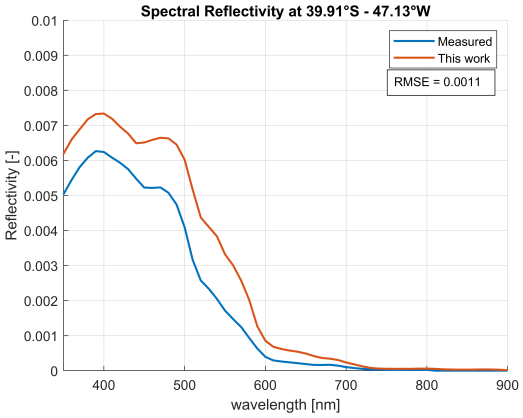
Spectral Reflectivity at 39.91°S - 47.13°W
Measured
This work
RMSE = 0.0011
Reflectivity [-]
wavelength [nm]

(e)

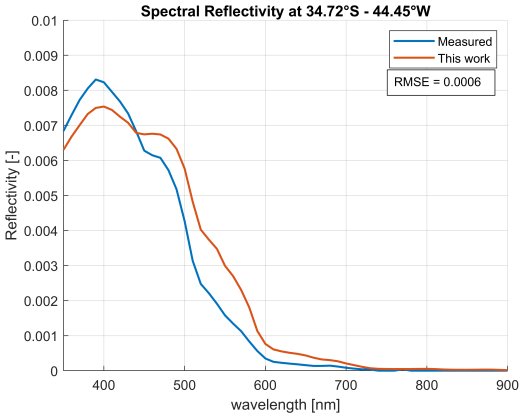
Spectral Reflectivity at 34.72°S - 44.45°W
Measured
This work
RMSE = 0.0006
Reflectivity [-]
wavelength [nm]

(f)

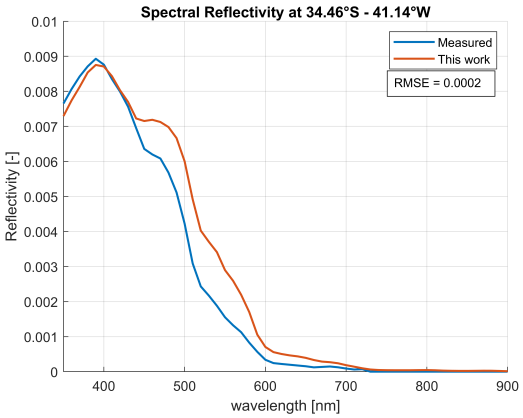
Spectral Reflectivity at 34.46°S - 41.14°W
Measured
This work
RMSE = 0.0002
Reflectivity [-]
wavelength [nm]

(g)

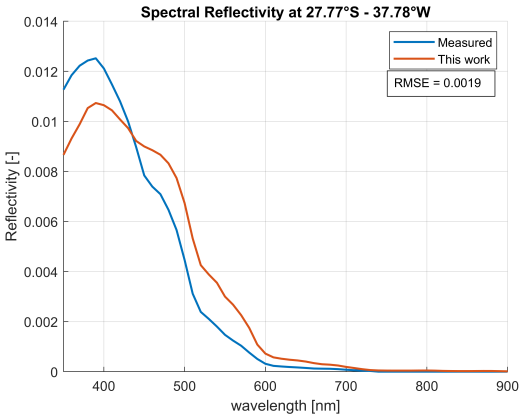
Spectral Reflectivity at 27.77°S - 37.78°W
Measured
This work
RMSE = 0.0019
Reflectivity [-]
wavelength [nm]

(h)

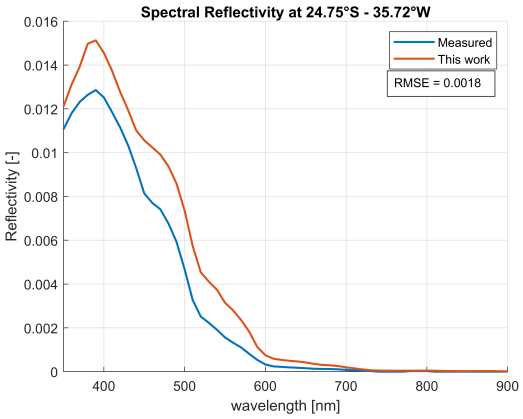
Spectral Reflectivity at 24.75°S - 35.72°W
Measured
This work
RMSE = 0.0018
Reflectivity [-]
wavelength [nm]

(i)

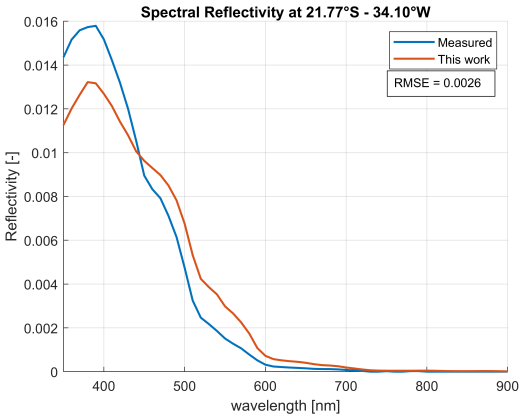
Spectral Reflectivity at 21.77°S - 34.10°W
Measured
This work
RMSE = 0.0026
Reflectivity [-]
wavelength [nm]

(j)

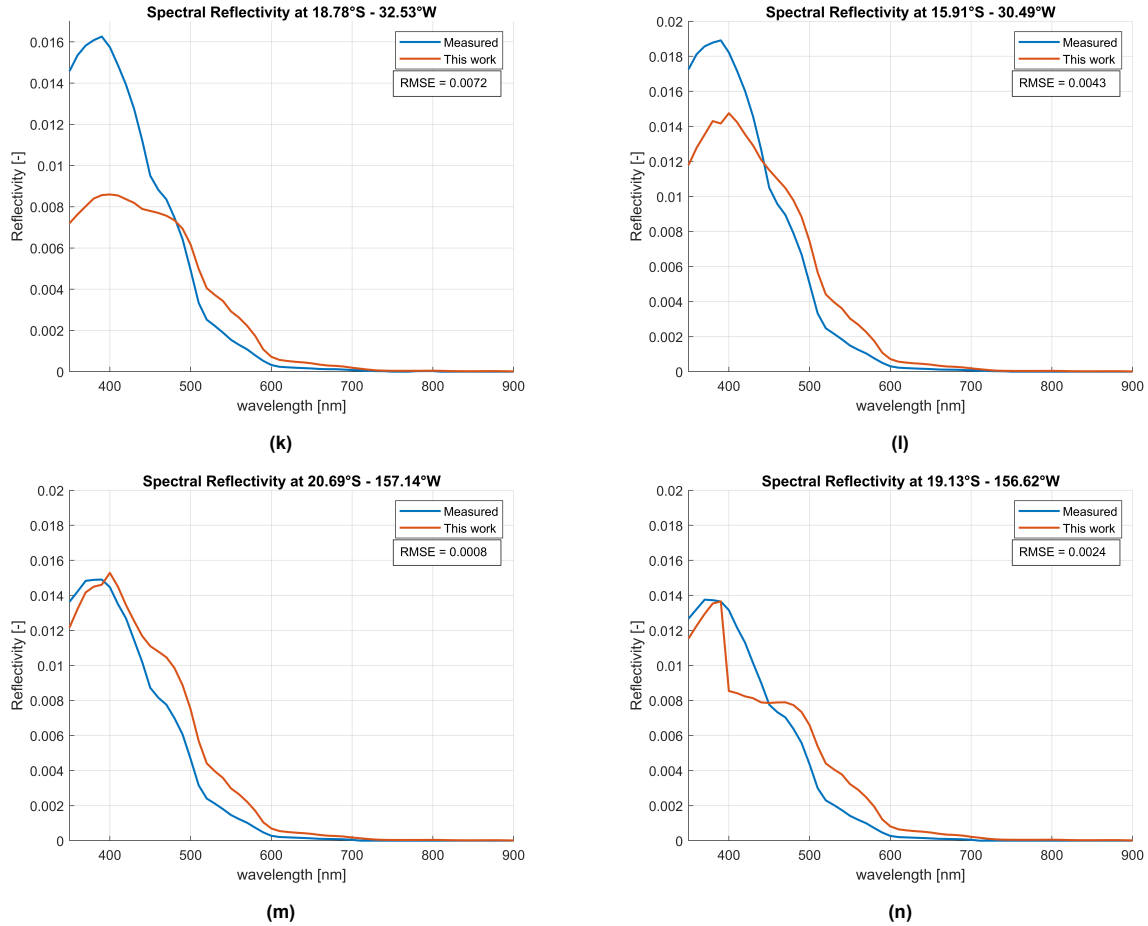

Figure 3.13: Numerical validation of GenPro4 model results ('This work') against dataset 1 ('Measured') for clear waters

In all datasets tested, the simulation follows the trend of the real data, and the RMSE values obtained are relatively low, indicating a reliable model to estimate the subsurface reflectivity.

The difference in spectral reflectivity between different graphs does not illustrate a consensus. While in some plots the simulation overestimates the real spectra (b-c-d-e from Figure 3.13), in others, an underestimation is obtained (j-k-l from Figure 3.13). Because the absorption and backscattering coefficients are extracted from dataset 1, the origin of the mismatch in the plots can have two potential origins.

First, the backscattering coefficient of mineral particles is calculated by using Equation 3.6, which in turn depends on the factor γ. Despite the fact that a value γ = 1 is widely used, this parameter is location-dependent [44], producing different exponential decay curves, modifying the curve obtained from Equation 3.8. Second, the factor $\frac{f}{Q}$ is an empirical variable as well, whose value depends on the waterbody treated, ranging from 0.08 to 0.12 [46].

Selecting more appropriate values for γ and $\frac{f}{Q}$ requires detailed experimental characterization of the waterbody properties, which falls outside the scope of this work. Given the low RMSE values achieved during the validation against dataset 1, the GenPro4 model, with the addition of backscattering effects, provides an accurate estimate of spectral reflectivity in low-turbidity waterbodies.

3.4. Comparison with dataset for turbid waters

The 14 data points tested in the previous section belong to a set of clear waterbodies characterized by low turbidity. Under these conditions, the overall albedo is driven mostly by interface reflectivity as the

water-leaving irradiance is quite low due to the small concentration of particles in water.

It is of interest in this work to evaluate how accurately the physical representation of spectral reflectivity caused by backscattering performs in turbid waters, where spectral reflectivity becomes more dependent on subsurface dynamics. Such turbidity increases the complexity of the radiative phenomena, as both particles and organic compounds increase their concentration, leading to different spectral reflectivity curve shapes.

Dataset 2 provides measurements from 5 specific locations known for their high turbidity. In this case, the spectral reflectivity, accounting for both subsurface contribution and the air-water interface, is measured directly. Then, it is possible to combine the GenPro4 simulation with the physical model and have a better understanding of the overall phenomenon. However, in this dataset, only the values of downwelling irradiance ($E_d(\lambda)$), upwelling irradiance ($E_u(\lambda)$), and turbidity (TSM) are reported. From the first two values, it is possible to calculate the effective spectral reflectivity (see Equation 3.1), but additional information from external sources is required to obtain the absorption and backscattering coefficients.

In the case of the absorption coefficient, the values of a_{ph} are obtained based on chlorophyll concentration data extracted from the Copernicus website. For the cases of a_{CDOM} and a_{NAP}, the values are obtained from the Copernicus website as well, which provides these values measured at 440nm [47]. To calculate the rest of the spectra, Equation 3.10 and Equation 3.11 are used.

$$a_{CDOM}(\lambda) = a_d(440) \cdot exp(-S_d \cdot (\lambda - 440)) \tag{3.10}$$

$$a_{NAP}(\lambda) = a_g(440) \cdot exp(-S_g \cdot (\lambda - 440)) \tag{3.11}$$

The variables S_d and S_g are obtained from [48] and [49], respectively.

To derive the backscattering coefficient, empirical relationships between particle concentration g/m^3 and particle-specific backscattering coefficient m^2/g are required. This formula is usually established at backscattering coefficients measured at large wavelength values due to their better stability compared to shorter wavelengths, which tend to vary more. A constant coefficient of $b^*_{bp}(680) = 0.009\ m^2/g$ measured at 680 nm is widely used to relate both variables [50]. Then, the backscattering coefficient is obtained according to Equation 3.12.

$$b_{bp}(680) = b^*_{bp}(680) \cdot TSM \tag{3.12}$$

The rest of the values of the spectrum are computed using Equation 3.6 and considering a value of γ = 1, like in the previous case.

Since the absorption coefficients required for the calculations must be obtained from an external source, an additional filter is applied to dataset 2 to include only data points with corresponding entries on the Copernicus website. Because many of these locations are near the coast, most were unavailable in the Copernicus database, which contains limited data for coastal regions. As a result, only 4 out of the 5 locations met the filtering criteria and contained valid absorption coefficient data. These four locations are therefore selected for the simulation, and the chosen data points used for validation are shown in Figure 3.14

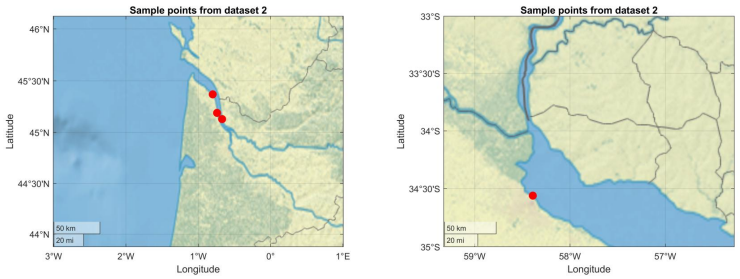

Latitude [°]	Longitude [°]
45.36	-0.80
45.12	-0.67
-34.56	-58.39
45.19	-0.74

Figure 3.14: Datapoints for model validation on the coast of France (left) and Argentina (right)

Table 3.4 shows the input data to perform the calculations to estimate the spectral reflectivity in each location. In this case, the data point located at 45.36°S - 0.80°W is selected. As the dataset offers data up to 1300 nm, the absorption and backscattering coefficients are also considered up to this wavelength. In the penultimate row of the table, the result given by GenPro4 is tabulated ($R_{interface}$). Considering that the devices used to measure the reflectivity have a length scale of centimeters, just like in the case of clear water, a flat surface is considered in the simulation, avoiding any roughness that could affect the results.

	400	500	600	700	800	900	1000	1100
a_{CDOM}	2.7457	6.6770	0.1669	0.0411	0.0101	0.0025	0.0006	0.0001
a_{chl}	0.0361	0.0009	0.0060	0.0001	0	0	0	0
a_w	0.0173	0.0256	0.2388	0.6481	2.068	6.776	35.42	19.3
b_{bp}	1.8232	1.4585	1.2154	1.0418	0.9116	0.8103	0.7292	0.6629
b_w	0.0037	0.0014	0.0007	0.0003	0.0002	0.0001	0.0001	0.0001
R_{bulk}	0.0434	0.0742	0.0821	0.0662	0.0335	0.0117	0.0022	0.0036
$R_{interface}$	0.0221	0.0210	0.0203	0.0199	0.0196	0.0194	0.0190	0.0186
R_{data}	0.0464	0.0884	0.1373	0.1286	0.0739	0.0323	0.0134	0.0166

Table 3.4: Spectral data table presenting absorption and backscattering coefficients, and reflectivity extracted from dataset 2.

The table contains the results of spectral reflectivity in the subsurface and also at the interface. By summing these two variables, the total value of the simulation is obtained and then compared with the real data measured. The results of both data and simulations are plotted in Figure 3.15.

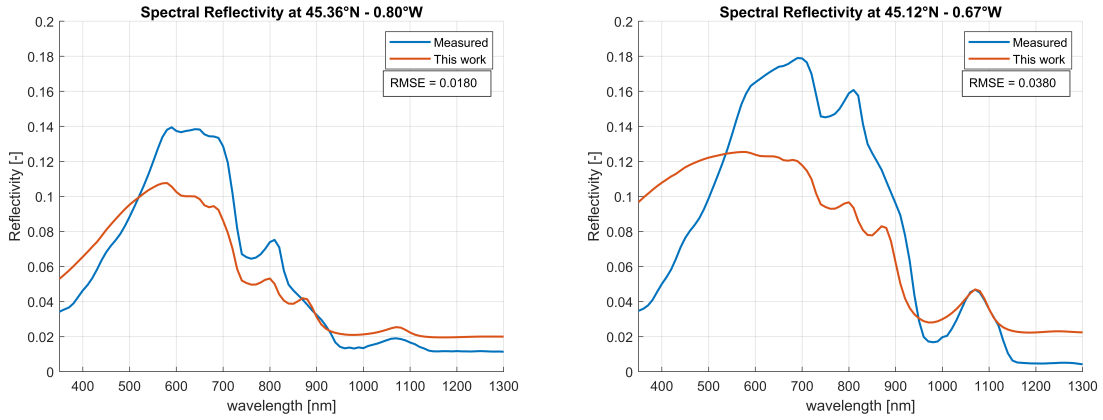

(a) turbidity = 126.57 g/m^3

(b) turbidity = 674.3 g/m^3

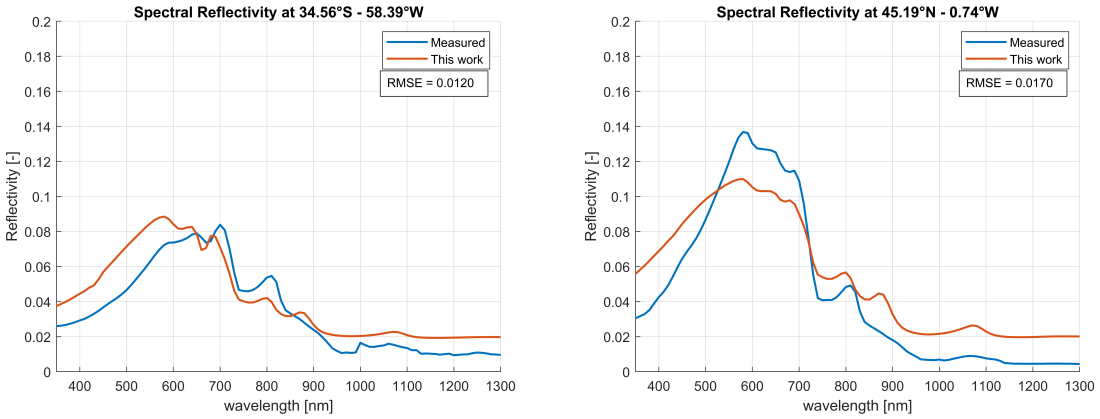

(c) turbidity = 60 g/m^3 **(d)** turbidity = 146.33 g/m^3

Figure 3.15: Spectral reflectivity simulated via physical + GenPro4 model vs measured data

From the four plots shown, it is possible to determine again a trend that follows the spectrum of real data, even when including the effect of the interface. This represents a good complementary relationship between both interface and bulk reflectivity models considered in Figure 3.12, ensuring the fit between both results.

Nevertheless, there are two important limitations to be analyzed. First, there is a significant mismatch in the region 500-700nm where backscattering effects find their maximum. In most of the cases, the simulation underestimates the actual value, leading to the hypothesis that the backscattering coefficient may not be fully accurate. This has its origin in the empirical approach chosen, especially in the factor γ (see Equation 3.6). Although its parameter is often assigned as 1, the real value is geographic-dependent, becoming an empirical variable [44].

Second, incorporating interface reflectivity enhances the overall curve fit but introduces discrepancies beyond 1000nm. In this range, the contribution from bulk reflectance becomes negligible, making spectral reflectivity dependent primarily on interface effects. While simulations yield a consistent 2% reflectivity assuming a flat surface, measurements vary from 0.3 to 1.6%, mainly due to inherent sea surface roughness that prevents a perfectly flat interface

Finally, by analyzing the RMSE values of the plots, there is a direct relationship between the turbidity of the waterbody and the RMSE obtained, as shown in Figure 3.16, indicating that higher turbidity leads to greater deviations between simulated and measured reflectivity.

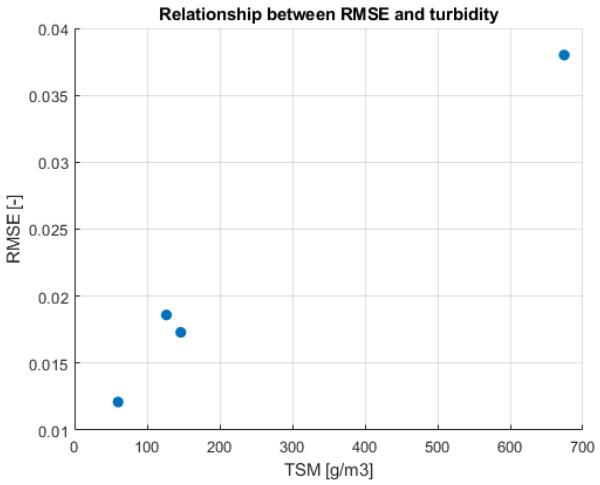

Figure 3.16: Relationship between RMSE and turbidity of the waterbody in each data point of dataset 2.

The lowest RMSE value is obtained in the case with the lowest turbidity (RMSE = 0.012 - Turbidity = 60g/m^3), while the largest RMSE coincides with the greatest turbidity registered (RMSE = 0.038 - Turbidity = 674.3 g/m^3), implying a loss of accuracy in the physical model when increasing the turbidity of the waterbody. It is important to note, however, that the data points studied in this case represent extreme scenarios of turbidity. Most of the waterbodies, including coastal zones as well, have TSM values below 100 g/m^3. In such cases, the RMSE obtained is approximately 0.01, demonstrating that the model provides a reliable and accurate approximation of the subsurface reflectivity and confirming that GenPro4 can simulate such conditions effectively.

3.5. Conclusions of Chapter 3

The goal of this chapter was to address the second research question: **To what extent does the GenPro4-simulated OSA agree with real measurements?** First, a preliminary validation showed strong agreement between GenPro4 albedo values and the Séférian empirical model.

Next, a numerical validation demonstrated that the initial version of the GenPro4 model exhibited several limitations. While it was suitable for modelling reflectivity associated with the interface between the waterbody and the atmosphere, it failed when simulating the subsurface dynamics due to the angular nature of backscattering that cannot be simulated via 1D models.

To address this limitation, a physical approach described on Equation 3.8 was introduced in the main model as a more suitable framework to characterize the subsurface dynamics. The results with the improved version of the GenPro4 model in both cases, clear and turbid water conditions, showed a strong agreement with the measurements of reflectivity registered in datasets 1 and 2. This indicates that the improved model provides a more realistic and reliable representation of the phenomenon. In all evaluated cases, the simulated reflectivity followed the trends observed in the measured data, and the (RMSE) values obtained were generally low: 0.72% for clear and 3.8% for turbid waterbodies, further supporting the validity and overall effectiveness of the proposed approach.

In the specific case of turbid waters, the accuracy of the improved GenPro4 model was found to be dependent on the concentration of suspended particles in the water column. Higher turbidity levels were associated with increased RMSE values, implying an upper turbidity threshold beyond which the accuracy of the model starts to decrease. Nevertheless, extremely high values of turbidity, such as 674 g/m^3, are rarely encountered in normal environments, and they are typically present in specific estuaries or certain lakes, which represent a small fraction of global waterbodies.

This numerical validation allows us to conclude that the improved version of the GenPro4 model presents a robust and reliable computational tool for calculating spectral reflectivity in aquatic environments. especially in clear waterbodies with low to moderate levels of turbidity.

4

Numerical Simulation of Representative Case Studies

This chapter addresses the third and final research question: How does the OSA change under different scenarios, and how do those changes affect the bifacial gain in offshore floating photovoltaic systems?

In the previous chapter, a robust model for calculating ocean surface albedo (OSA) was developed and tested under different scenarios, demonstrating a strong fit with real data, both interface and sub-surface reflectivity. This model can now be applied to simulate different sea states and assess how strongly each parameter influences albedo. From the past chapters, we know that factors such as waves, organic material, and mineral particles play significant roles in albedo calculations. Identifying under which conditions each parameter becomes more or less influential is essential for explaining the mechanisms behind bifacial gain in offshore floating photovoltaic (OFPV) plants.

Waterbodies around the world can be turbulent or calm, turbid or clear. Each of these conditions exhibits different values of albedo, since the parameters that define the spectral reflectivity differ from case to case. It is therefore necessary to analyze different scenarios and identify the key parameters that affect OSA in order to determine suitable locations for the installation of OFPV plants from an energy generation perspective.

In the following chapter, section 4.1 describes the methodology used to integrate the outputs from the improved GenPro4 model into the PVMD TOOLBOX developed at TU Delft. Next, section 4.2 examines the key factors behind OSA calculations and establishes a prioritization of such variables according to their influence on OSA. Finally, section 4.3 evaluates the GenPro4 model proposed in realistic sea state regimes generated using data extracted from the Copernicus website. This is to gain further insight into the bifacial gain variations at a global scale and analyze their impact on the levelized cost of electricity (LCOE).

4.1. Experimental Design and Simulation Workflow

4.1.1. TOOLBOX modifications

The PVMD TOOLBOX [51] is a program developed at TU Delft that models and predicts the energy performance of photovoltaic (PV) systems under different scenarios. This tool enables the estimation of the energy yield for PV systems under various environmental conditions, allowing the assessment of how the factors that define such an environment influence power generation.

The basic workflow of this tool is detailed in Figure 4.1.

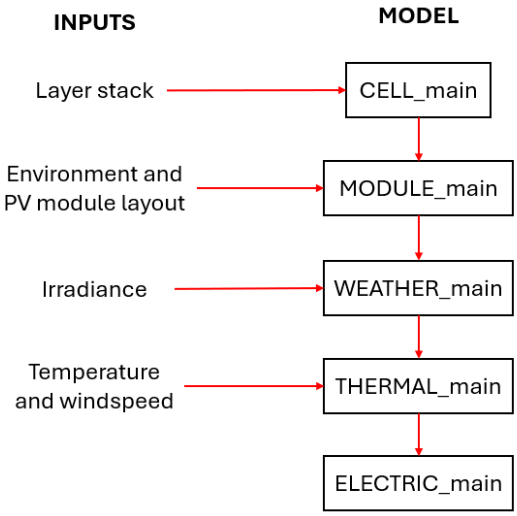

Figure 4.1: TOOLBOX basic flowchart defining each main function inside the main computational tool.

Currently, the program allows for the calculation of PV performances under different environments, where the geometry and the albedo of the surface can be modified. Nevertheless, this albedo is defined as a constant over the entire wavelength spectrum and time, which is not correct in the case of offshore environments. Consequently, a different approach is required to integrate the results coming from the GenPro4 model.

For OFPV plants, the environment corresponds to the sea profile, which is defined in PVMD TOOLBOX as a discrete geometry consisting of triangular faces that emulate the shape of waves. To include the spectral variability of reflectivity in this environment, a set of modifications are applied to the PVMD TOOLBOX, which are detailed in Appendix C. Consequently, the initially constant value of albedo becomes an $m \times n$ matrix (m is the number of wavelength samples and n is the number of triangular faces used to define the sea profile).

A fraction f_{wc} of these n faces represents whitecaps, randomly distributed over the ocean area of the simulation, and is therefore assigned the spectral reflectivity of whitecaps. The remaining fraction $(1 - f_{wc})$ is assigned the spectral reflectivity of the wavy water calculated using GenPro4.

With this procedure, the environmental albedo is fully defined and incorporated into the main workflow of the PVMD TOOLBOX.

4.1.2. Simulation WorkFlow

PVMD TOOLBOX can now work with spectral reflectivities defined for faces representing whitecaps or water. Nevertheless, it is necessary to address how the interface and bulk reflectivity are calculated and then incorporated into the main workflow of PVMD TOOLBOX, as presented in Figure 4.2.

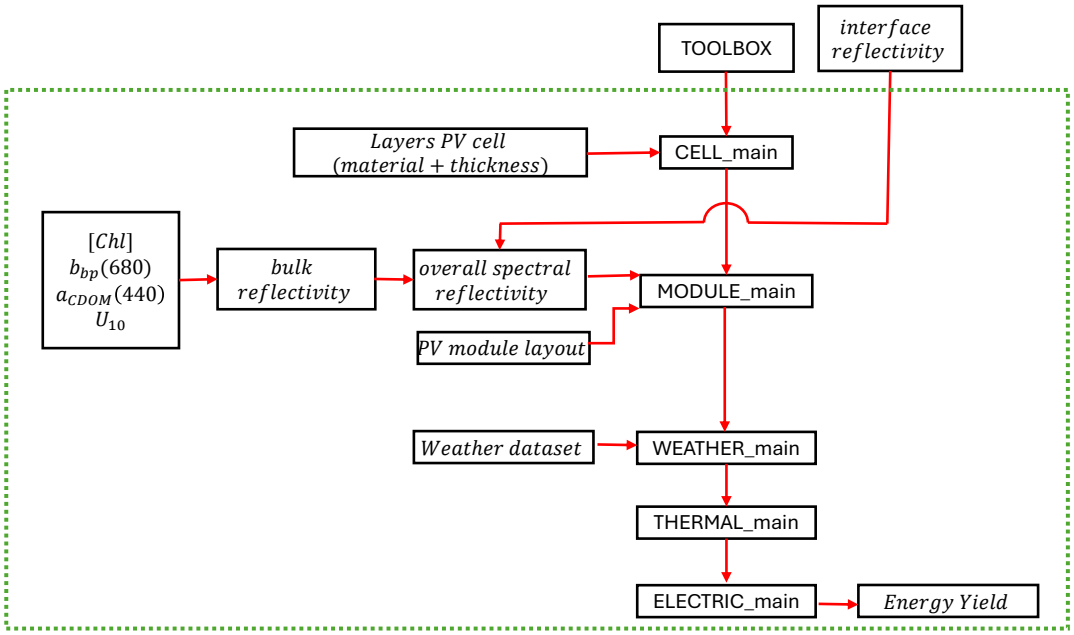

Figure 4.2: Overall Workflow of PVMD TOOLBOX with auxiliary codes for the obtention of energy yield.

In the case of interface reflectivity, given a certain location defined by a specific latitude and longitude, the sea profile must be defined throughout the significant wave height (H_s) and the peak period (T_p) that are selected based on the target wave scenario to be simulated.

This (H_s, T_p) pair is linked to a specific energy density spectrum ($E(f, \theta)$) that provides the wave profile of the waterbody via Equation 1.10. With this already defined, the GenPro4 model can be executed to obtain the interface reflectance.

For all simulations, the wavelengths span from 300 nm to 1200 nm, with a resolution of 20 nm. The layers cover an area of 25x25 m, and consist of:

- top semi-infinite layer of air.
- an intermediate layer of water of 100 m with a wave profile at the top
- a semi-infinite bottom layer of seabed represented by clay [33].

The case of bulk reflectivity is calculated inside the PVMD TOOLBOX loop as illustrated in Figure 4.2. The procedure for including the parameters that define subsurface reflectivity (absorption and backscattering coefficients), along with wind speeds to define whitecap coverage are detailed in Appendix C.

These modifications implemented to the PVMD TOOLBOX allow for the calculation of the energy yield of OFPV systems under realistic scenarios of OSA. From here, the bifacial gain can be calculated using Equation 1.1, providing a numerical value to the optimization of power output when using bifacial panels.

4.2. Single-factor Sensitivity Analysis

As discussed throughout this research, spectral reflectivity is a multivariable function. It depends on multiple parameters that are, to a certain extent, interdependent. Therefore, quantifying the contribution of each parameter to ocean surface albedo is crucial since optimal values for all parameters rarely coincide at a single location. This makes it necessary to prioritize certain parameters based on specific criteria.

This section evaluates the four main variables involved in the sea optical phenomenon to quantify their relative impact on OSA calculations. Each variable is varied over a range representative of natural waterbodies.

This sensitivity analysis starts from a reference ("baseline") case, in which all variables are assigned standard values. Such parameters are:

- Whitecaps: Defined by wind velocity measured 10 m above the sea surface in m/s (U_{10}).
- Chlorophyll Concentration: Measured in mg/m^3 ($[Chl]$).
- Mineral Particle Concentration: Measured in g/m^3 (TSM).
- Sea Roughness: Defines wave geometry. It is commonly described with the significant wave height in m (H_s) linked to a specific peak period in s (T_p).

From this baseline case, each variable is varied independently in a certain range to evaluate the individual impact on the results.

Fully developed open oceans with low concentrations of organic and inorganic material are the predominant sea state globally. The baseline case is established in the North Sea at the coordinates 55°N - 5°E, as it is a close representation of fully developed waterbodies with low turbidity. Then, for this specific location, the default values of the variables considered are summarized in Table 4.1.

Variable	Value
Wind Speed (U_{10})	10 m/s
Chlorophyll Concentration ($[Chl]$)	0.05 mg/m^3
Mineral Particle Concentration (TSM)	0.5 g/m^3
Significant Wave Height (H_s)	2 m
Peak Period (T_s)	10 s
Tilt Angle	40°

Table 4.1: Variable values to represent the default case of the study.

The primary metric for comparison is the **yearly bifacial gain** described in Equation 1.1, which quantifies the additional energy that is generated (or lost) when varying these variables independently. Each case is tested using the PVMD TOOLBOX [51] to obtain the annual energy yield for both monofacial and bifacial PV modules, from which the bifacial gain is determined.

For simplicity, a single PV module is tested, corresponding to a 12x6 cell configuration, whose composition, in the case of the monofacial module, is illustrated in Figure 4.3 and detailed in Table 4.2.

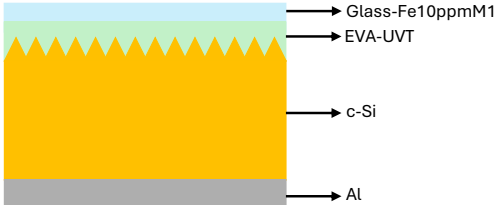

Figure 4.3: Schematic representation of the monofacial PV cell to be tested.

Layer	Thickness (µm)
Glass-Fe10ppmM1	2500
EVA-UVT	450
c-Si	160
Al	20

Table 4.2: Composition of monofacial PV cell tested using PVMD Toolbox.

For the bifacial module, to maintain comparable optical characteristics, the cell is represented as a mirrored configuration of the monofacial cell. This approach minimizes the performance difference coming from different materials or textured surfaces, ensuring equivalent conditions for the simulations. Consequently, the composition of the bifacial cell used in the computational experiment is illustrated in Figure 4.4 and detailed in Table 4.3.

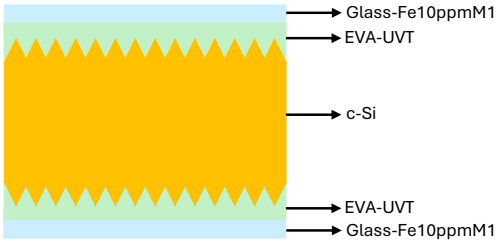

Figure 4.4: Schematic representation of the bifacial PV cell to be tested.

Layer	Thickness m
Glass-Fe10ppmM1	2500
EVA-UVT	450
c-Si	160
EVA-UVT	450
Glass-Fe10ppmM1	2500

Table 4.3: Composition of bifacial PV cell tested using PVMD TOOLBOX..

In both cells, a texture is placed at the top (and rear for the bifacial cell) consisting of a pyramidal texture with a mean roughness of 20 µm.

For each parameter to be studied, the variables listed in Table 4.1 are set according to the workflow defined in subsection 4.1.2, while the target parameter is varied across a certain range. The results of this sensitivity analysis are presented below.

4.2.1. Whitecaps

As highlighted in the literature review, the presence of foam created by waves breaking in the ocean increases OSA, since its intrinsic spectral reflectivity is higher than that of seawater. Nevertheless, its influence is affected by another important parameter: whitecap coverage.

Although waves are continuously breaking, the foam produced covers only a small portion of the sea area, commonly determined by the local wind speed (Equation 1.14).

Starting from the default case described in Table 4.1, only the wind speed is varied in increments of 5 m/s, ranging from 0 to 25 m/s. The upper limit of 25 m/s is chosen because it represents the typical upper limit of windspeed that most of the OFPV systems withstand without compromising the energy output. This upper limit of wind velocity leads to a maximum whitecap coverage of 6.63% according to Equation 1.14.

The rest of the resulting whitecap coverages are shown in Table 4.4

Wind velocity (U_{10} m/s)	Whitecap coverage (f_{wc}) %
0	0.00
5	0.51
10	1.54
15	2.94
20	4.65
25	6.63

Table 4.4: Whitecap associated with different wind speed regimes.

Then, a total of six simulations are carried out, leading to six different sea states with the same wave profile but with different whitecap coverage, as it is shown in Figure 4.5.

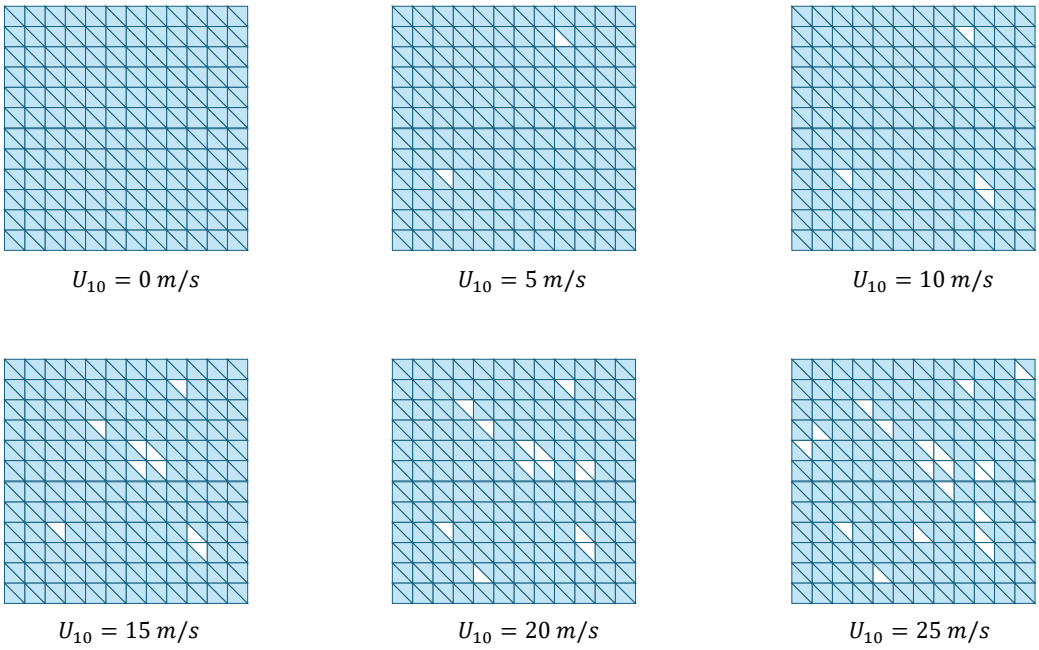

Figure 4.5: Top view of sea states simulated with f_{wc} = 0% at 0 m/s, f_{wc} = 0.51% at 5 m/s, f_{wc} = 1.54% at 10 m/s, f_{wc} = 2.94% at 15 m/s, f_{wc} = 4.65% at 20 m/s, and f_{wc} = 6.63% at 25 m/s,.

Figure 4.5 shows the triangular sea environment created in PVMD TOOLBOX under different wind speed regimes. Higher wind speeds increase whitecap coverage on the sea surface. This raises the overall albedo because whitecaps have higher spectral reflectivity than the surrounding water. This albedo increase should raise the annual energy yield calculated. Quantifying this gain is crucial to determining the importance of this parameter in the proposed model.

Whitecaps form randomly on the sea surface, which affects OSA. If foam appears directly beneath a PV module, it alters OSA differently than when this foam is placed farther away. To attenuate the noise generated by the random location of whitecaps, multiple simulations are averaged for each wind speed. This produces more reliable results that can be compared across different wind scenarios. Therefore, 5 simulations are executed for each wind speed, obtaining different whitecap distributions with the same coverage. The average result of these 5 simulations is used for comparison with other wind conditions.

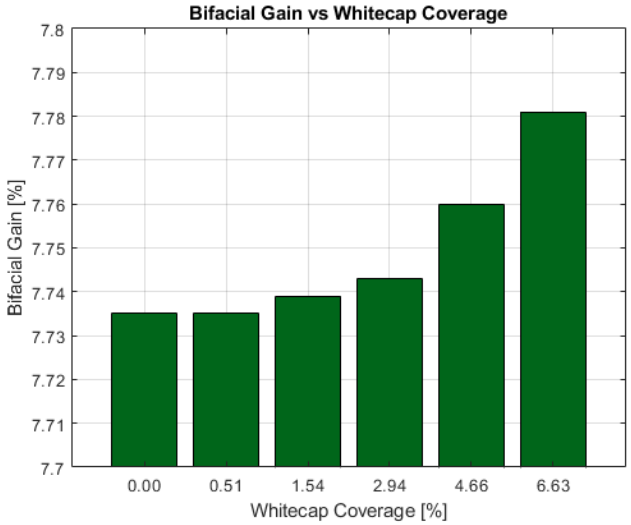

Figure 4.6: Bifacial Gain under different whitecap coverage scenarios

Figure 4.6 exhibits a clear trend: bifacial gain increases whitecap coverage. This makes sense because foam has a higher reflectivity spectrum compared to seawater. However, the magnitude of this change remains low. Varying the wind conditions from 0 m/s to 25 m/s raises the yearly bifacial gain just 0.045%, which is a negligible change considering the scenario range.

While the whitecap coverage varied from 0% to almost 7%, random whitecap distribution dilutes its impact, since they are rarely located directly under the PV modules. Furthermore, because a single PV module is tested in these simulation the rear side area is considerably low, reducing whitecap's impact as well. The rear side of the PV module thus sees a mix of foam/seawater environment, where the average reflectivity is strongly dominated by seawater. Then, whitecap coverage becomes a minor parameter for OSA calculations.

4.2.2. Chlorophyll

Chlorophyll levels remain low across most oceanic waterbodies, but natural variability affects subsurface optical properties and, consequently, OSA values. Understanding this parameter's role is key, as chlorophyll concentrations are often waterbody specific, helping to select locations with optimal chlorophyll concentration that maximizes OSA.

The maximum value of chlorophyll concentration occurs in estuaries and coastal zones in latitudes close to the Equator, peaking near Perú's coast at 3 mg/m^3. Then, this value will be used as the upper limit in the sensitivity analysis, and six different cases will be tested under concentrations of 0.05, 0.1, 0.5, 1.0, 2.0, and 3.0 mg/m^3. while holding the rest of the variables at the default values set in Table 4.1.

Though coloured dissolved organic matter (CDOM) and non-algal particles (NAP) also affect subsurface optical dynamics, chlorophyll's impact dominates in most cases. For simplicity, only the effect of chlorophyll is analyzed as the key organic factor.

Yearly PVMD TOOLBOX simulations are executed for both bifacial and monofacial cases, allowing us to get the effects of chlorophyll on the bifacial gain when isolating this variable.

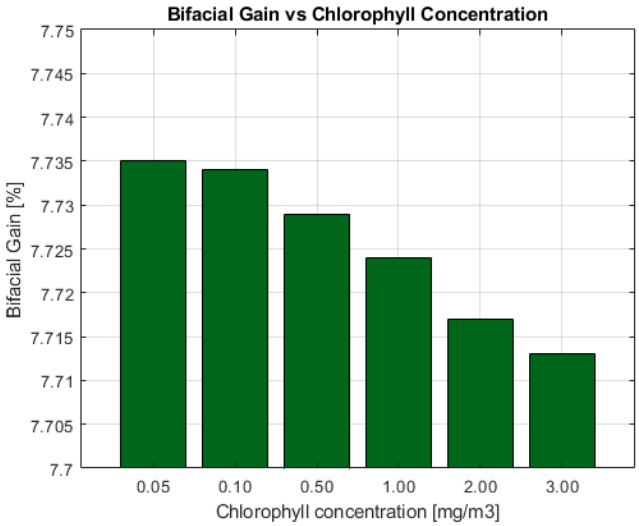

Figure 4.7: Bifacial Gain under different chlorophyll concentration scenarios

According to Figure 4.7, an increase in chlorophyll concentrations is linked to a reduction in the overall bifacial gain. This aligns with the physical model employed (see Equation 3.8), where chlorophyll primarily boosts absorption in the water column.

More absorption means less light being reflected upwards because of energy conservation, as it is shown in Equation 4.1.

$$A + R + T = 1 \tag{4.1}$$

Consequently, higher concentrations of chlorophyll lead to lower reflectivity results, reducing the bifacial gain.

However, this reduction is on the order of 0.02%, which is a negligible change considering that this parameter was varied from very low concentration regimes (0.05 mg/m^3) up to rich-chlorophyll scenarios present commonly in estuaries and certain coastal zones (3 mg/m^3).

This negligible effect confirms that this parameter does not play an important role in sea reflectivity, as its contribution centers on absorption rather than reflection.

4.2.3. Mineral Particles

This element is associated with backscattering, which is the main driver of subsurface albedo, as discussed previously. Together with chlorophyll, they govern the subsurface optics of waterbodies.

Nevertheless, unlike the organic component, the variability of this parameter is much higher, spanning values between 0.1 and 1 g/m^3 in open waters to values as high as 100 g/m^3 in estuaries and nearshore zones. Due to this broad range, concentrations are tested logarithmically: 0.1, 0.5, 1, 10, 50, and 100 g/m^3. This spans open seas (0.1-1 g/m^3), coastal zones (10 g/m^3), and estuaries (50-100 g/m^3).

All other parameters, including the wave profile defined by H_s and T_p, remain constant. Taking this into consideration, the simulation results are shown below.

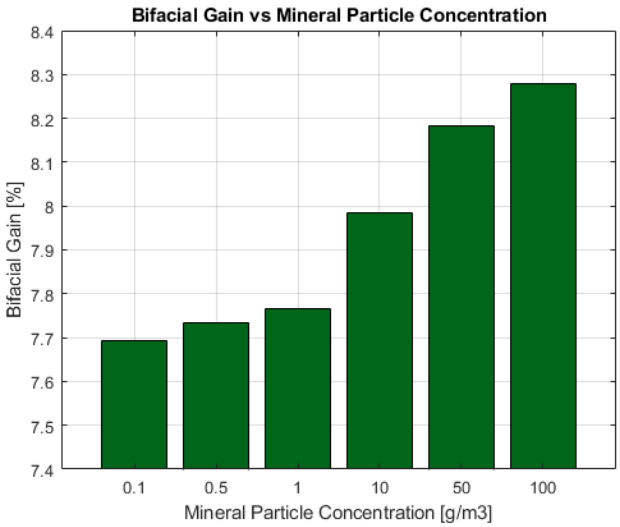

Figure 4.8: Bifacial Gain under different particle concentration scenarios

Figure 4.8 shows a clear trend to increase the bifacial gain when the subsurface becomes more turbid. This is explained by Equation 3.8, where higher mineral particle concentrations boost backscattering and thus subsurface reflectivity (see Equation 3.12).

The total change between the extreme cases reaches about 0.6%, which is higher than the effect of chlorophyll. However, this percentage variation occurs only when comparing the extreme cases of clear waters versus highly turbid waterbodies that are rarely found in offshore locations.

Varying chlorophyll and particle concentrations in a waterbody, even in the most extreme cases, yields a bifacial gain change of less than 1%. Bulk reflectivity thus contributes to a low extent to the optical phenomenon.

In the previous chapter, bulk reflectivity notoriously impacted the spectral shape of reflectivity. However, as illustrated in Figure 4.8, its contribution to the yearly bifacial gain is overshadowed by another

variable involved in OSA estimates. The validation in Chapter 3 was conducted assuming flat seawater conditions (no waves), since the datasets used lacked information about this variable. Therefore, in the following subsection, the effect of sea roughness is examined to assess its influence on the bifacial gain.

4.2.4. Sea Roughness

Analyzing the effect of waves on OSA as an isolated factor represents a challenge because they are defined by two variables: the significant height (H_s) and the peak period (T_p). This implies that each sea state is associated with a unique pair (H_s,T_p).

This requires matrix results, with H_s and T_p spanning defined ranges based on extreme cases of each variable.

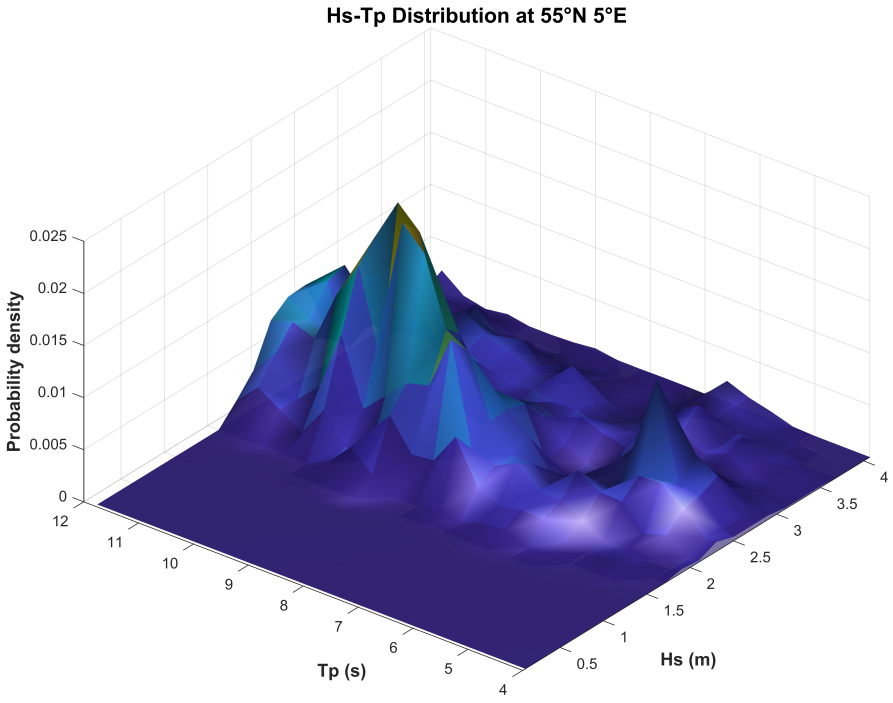

Figure 4.9: Distribution of (H_s,T_p) in hourly values over an entire year at the North Sea coordinates 55°N - 5°E.

Figure 4.9 presents a typical histogram that shows the frequency distribution of significant wave height and peak period at a specific location. From the plot, values of 4 or 5 m are rarely found, while 3 m represents an accurate maximum threshold for H_s.

The upper limit for H_s does not vary much, since it corresponds to a fully developed sea state (storms or extremely rough sea states are not present). Therefore, the (H_s) values selected for testing range from 0.5 to 3 m, 0.5 m representing a calm scenario and 3 m becoming the roughest possible scenario in fully developed sea states. Additionally, from the plot, T_p values of 8, 9, and 10 s are chosen for this sensitivity analysis as they possess the highest frequency of occurrence.

The results form a 4$\times$3 matrix (4 H_s and 3 T_p values). As in the previous cases, the bifacial gain is the key parameter for comparison, and the outcomes of these simulations are shown in Figure 4.10

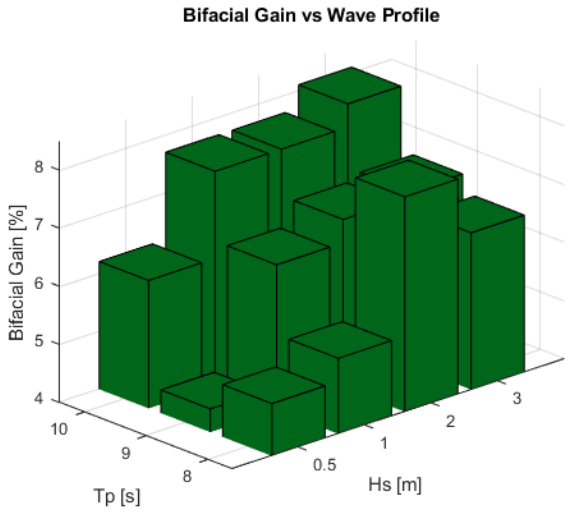

Figure 4.10: Bifacial Gain under different wave profile scenarios

The plot shows a trend to increase OSA when increasing H_s. Analyzing the significant wave height, larger values of this parameter produce steeper slopes that enhance interface reflection because of the optimal incidence angles achieved. The tested range of H_s values does not exceed the upper thresholds where excessive steepness causes light trapping, which reduces reflectivity (see Figure 2.7). Therefore, for H_s in a range of 0.5 - 3 m, higher values of this variable lead to a larger bifacial gain.

The effect of T_p is less consistent, and its influence is non-linear. Although a weak trend toward increased bifacial gain appears at higher T_p values, this relationship lacks regularity in the tested range. Consequently, this variable cannot be treated as an independent parameter since it does not provide a reliable trend in bifacial gain predictions.

A change in bifacial gain of almost 3.5% occurs between the extreme cases of the simulations plotted in Figure 4.10. Consequently, the wave profile becomes the main parameter that alters bifacial gain in offshore PV modules, producing higher outcomes at higher values of both H_s and T_p.

This serves as an indicator of the importance of interface geometry, as it overshadows the contributions of whitecaps, chlorophyll, and mineral particles.

4.3. Simulation of Realistic Ocean Regimes

The previous section provides insight into the influence of the parameters that determine ocean surface albedo. This analysis was conducted by varying one specific parameter while holding all remaining variables constant. In reality, all variables change dynamically over time. To simulate energy yields and, subsequently, bifacial gains, calculations must use the actual data available from the location of study.

A total of 4 different locations are selected to examine the variation of bifacial gain in each site using real data specific to the zone. The locations in this study form a considerably heterogeneous sample in terms of turbidity and sea state, since both near-coast areas and open oceans are considered.

The characterization of each area, the methodology of analysis, and the results obtained are discussed in the following subsection.

4.3.1. Analysis of Study Cases

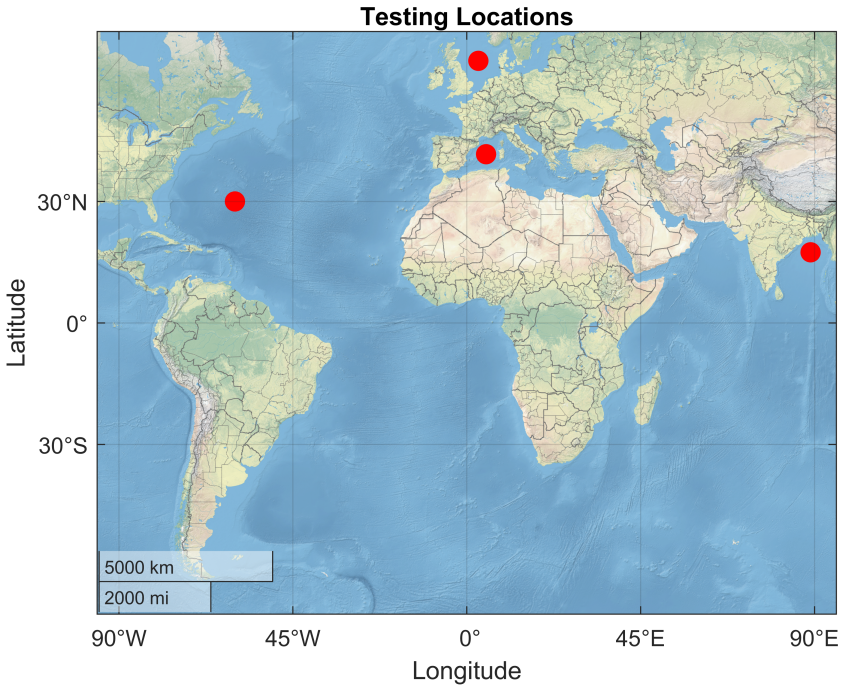

Figure 4.11: Coordinates of the four selected scenarios for yearly bifacial gain simulations.

Figure 4.11 illustrates the four locations where the bifacial gain is analyzed. These areas are briefly described below, highlighting the concepts of turbidity and sea states (wave profile).

- **Atlantic Ocean (30°N, 60°W)**: It represents a fully developed sea state with high waves. The turbidity phenomenon is characterized by a low concentration of mineral particles, since it is an offshore location far from the coast, and a low chlorophyll concentration driven by seasonal changes.
- **Mediterranean Sea (40°N, 5°E)**: It has a lower wave profile compared to the ocean cases, due to the semi-enclosed location leading to a shorter fetch of waves. Turbidity is slightly higher, and modest concentrations of chlorophyll are found with weak seasonal patterns.
- **North Sea (56°N, 3°E)**: Sea state dominated by moderate to high significant wave heights, with long fetch over the area. Turbidity caused by mineral particles is moderate because of resuspension of the sediments driven by local wind. Chlorophyll concentrations are low compared to the rest of the scenarios analyzed.
- **Indian Ocean (18°N, 89°E)**: Wave profile is strongly seasonal, marked by high and strong wave profiles during monsoon season, and calmer states in pre- and post- monsoon periods. There is a high turbidity caused by the river's inputs, and while chlorophyll concentrations are high along these river plumes, the concentration decays strongly when moving to offshore zones, which is the specific case of this location.

Like in the sensitivity analysis case, calculating a yearly energy yield is key to determining the bifacial gain across the entire year. Nevertheless, this approach seeks to provide a more realistic representation of the different ocean regimes found worldwide; therefore, daily data on chlorophyll concentration, mineral particles, colored dissolved organic matter (CDOM) concentration, and whitecap coverage are used in the simulations. This results in 365 different environments that must be accounted for in the PVMD TOOLBOX when running the model.

Each environment links to a unique day. The calculation of 365 simulations using PVMD TOOLBOX (730 in the case of bifacial modules) entails a high computational cost, since each environment simula-

tion requires about 1 minute to compute, which leads to 12 hours of computation for a single scenario. Since this section focuses on understanding the trend of bifacial gain during a year across different scenarios, selecting specific target days in the year creates a sufficiently robust sample to study the yearly trend while reducing computational costs. Thus, the 10th, 20th, and 30th days of each month (28th in the case of February) are chosen to create a sample dataset on which the simulation are run to analyze the behavior of the bifacial gain throughout the year. This implies a reduction from 365 to 36 simulations, thereby significantly reducing computational time while maintaining the aim of the section.

For each selected day, the daily energy yield is calculated for both monofacial and bifacial modules to enable subsequent comparisons. Following the procedure defined in subsection 4.1.2, each day, a unique environment is created based on the subsurface components and whitecap coverage ($[Chl]$, TSM, CDOM and f_{wc}); additionally, a fixed sea state is selected as representative of each location, using the modal value found in the histogram of the significant wave spectra and peak period (see Figure 4.9) specific for the study zone,

Such sea states, with their respective H_s and T_p values are illustrated in Figure 4.12

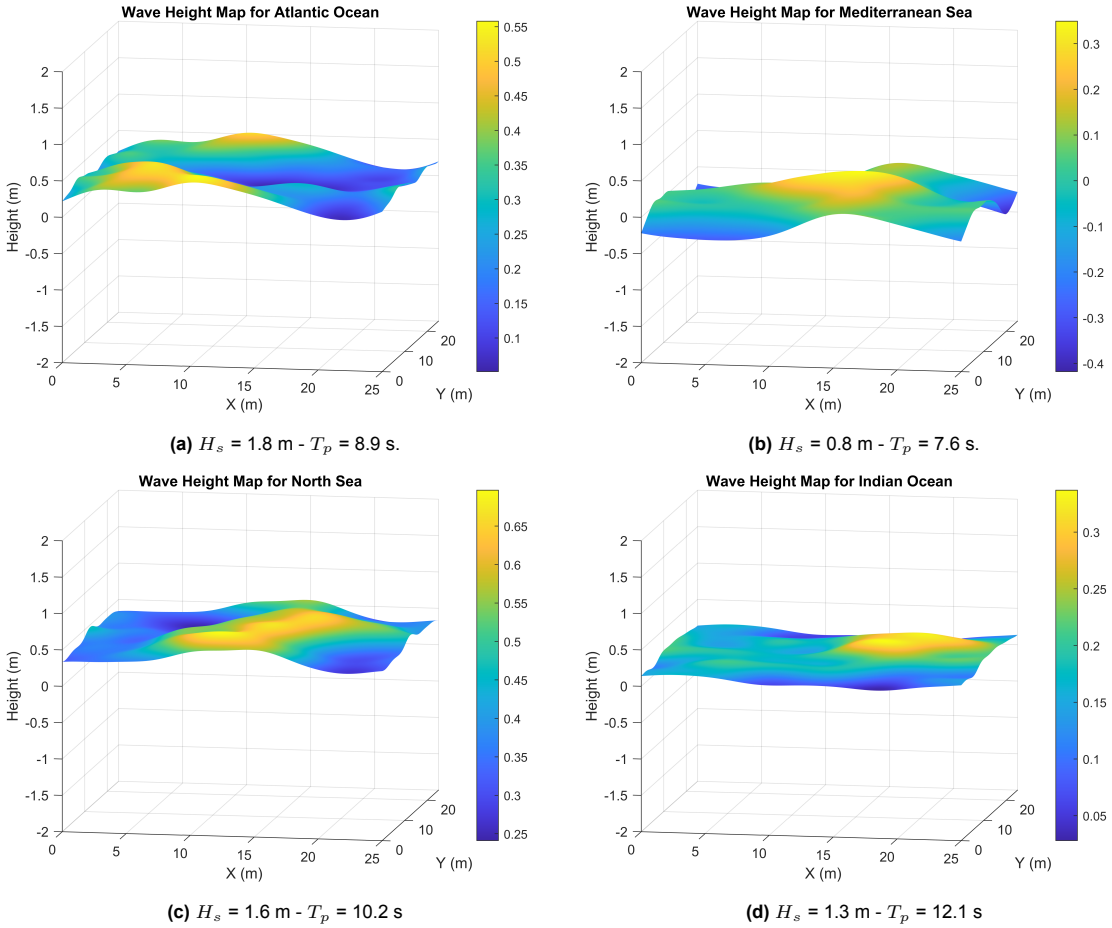

(a) H_s = 1.8 m - T_p = 8.9 s.

(b) H_s = 0.8 m - T_p = 7.6 s.

(c) H_s = 1.6 m - T_p = 10.2 s

(d) H_s = 1.3 m - T_p = 12.1 s

Figure 4.12: Representative sea states generated by modal values of H_s and T_p from each study location.

With this setup, the same workflow detailed in Figure 4.2 is applied for each of the 36 chosen days. This produces the daily energy yield for each selected date, creating a dataset of results to be studied and compared to analyze the bifacial gain over a full year.

The 36 daily bifacial gain values are grouped into monthly results. For each month, three representative daily values are shown in a box chart to present the variability within that month. Consequently, each location has a box chart with twelve components, representing the monthly and yearly variation of this parameter

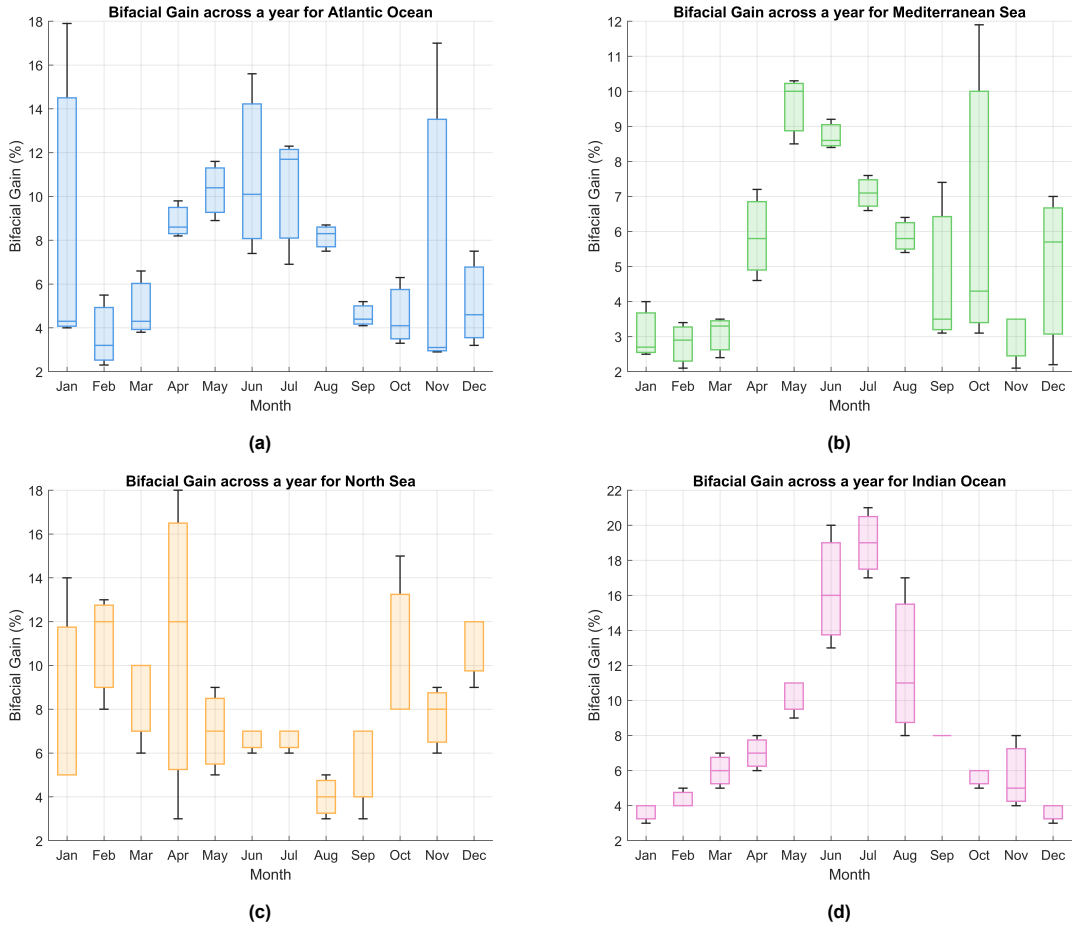

Figure 4.13: Bifacial gain variability across one year at multiple worldwide locations.

Figure 4.13 illustrates the trend of bifacial gain over an entire year, based on representative days selected for each month as previously described. The pattern resembles that of solar irradiance, peaking in summer times, and reaching low values during winter. This seasonal variation is more pronounced in locations near the Equator (Indian Ocean) and decays with increasing latitudes (North Sea).

Higher bifacial gains during summer are mainly due to solar altitude, which enhances the amount of radiation that reaches the sea surface, and consequently, boosts rear-side illumination. In contrast, on winter period, the lower solar altitude produces longer module shadows over the sea, reducing the albedo effects. Moreover, summer conditions are dominated by direct radiation, which allows larger reflectivity compared to winter, when diffuse radiation becomes more important, which is less effective for rear-side collection.

At higher latitudes, the greater air mass increases the fraction of diffuse radiation. Because diffuse radiation is isotropic and lacks a preferred direction, only a small fraction hits the rear side of the PV module, limiting reflectivity benefits.

Despite the seasonal and geographical variations, the resulting bifacial gain consistently provides a substantial power output improvement with the following mean values of bifacial gain per location.

- Atlantic Ocean - 6.7%
- Mediterranean Sea - 5.5%
- North Sea - 6.5%
- Indian Ocean - 7.5%

The fact that all locations exhibit an average bifacial gain in the range 5 - 8% demonstrates robust performance gains for offshore floating PV systems, highlighting the importance of dynamic OSA modelling in these simulations.

4.3.2. Bifacial vs Monofacial Implications

The bifacial gain of around 5 - 8% obtained above represents substantial enhancements in energy yield compared to the monofacial scenario. These improvements justify using bifacial modules in OFPV plants for better performance and potentially reduce costs.

Although the economic assessment of OFPV plants falls outside the scope of this study, a simplified analysis validates project viability. Generating between 5 - 8% more power only by implementing bifacial panels offers an attractive possibility to reduce the levelized cost of electricity (LCOE).

$$LCOE = \frac{CAPEX + \sum_{t=1}^{N} \frac{OPEX_t}{(1+r)^t}}{\sum_{t=1}^{N} \frac{E_t}{(1+r)^t}} \tag{4.2}$$

where:

- $CAPEX$: Capital expenditure,
- $OPEX_t$: Operations expenditure for the year t,
- E_t: Electricity generation in year t,
- r: Discount rate,
- N: Expected lifetime.

From Equation 4.2, only the variables of $CAPEX$ associated with the PV modules, and E_t linked to the power output vary. Bifacial modules are 10 - 20% more expensive than monofacial ones, and they often represent 30 to 40% of the overall $CAPEX$ [52].

For instance, assuming the bifacial modules to be 20% more expensive and representing 40% of the initial investment yields an effective $CAPEX$ increase of 8%, while a bifacial gain of 6% proportionally boosts power production. Thus, the LCOE expression for the case of bifacial modules is presented below.

$$LCOE = \frac{1.08 \cdot CAPEX + \sum_{t=1}^{N} \frac{OPEX_t}{(1+r)^t}}{\sum_{t=1}^{N} \frac{1.06 \cdot E_t}{(1+r)^t}} \tag{4.3}$$

The net effect on LCOE approaches breakeven or lower, as the full yield uplift offsets the partial $CAPEX$ rise.

OSA thus becomes a key factor for accurate LCOE projections in OFPV, since its impacte in the overall energy yield, via the bifacial gain factor, alters significantly the economic output of such analysis.

This simplified analysis demonstrates that power output gains from bifacial modules have the potential to mitigate their higher costs, achieving competitiveness. OSA emerges as a critical factor for accurate LCOE projections in OFPV, as it drives bifacial gain and thus overall economic viability.

4.4. Conclusions of Chapter 4

The third and final research question of this thesis: **How does the OSA change under different scenarios, and how do those changes affect the bifacial gain in offshore floating photovoltaic systems?** was addressed in this chapter. The GenPro4 model was executed to assess the bifacial gain in different predefined scenarios characterized by the variables treated in this work (chlorophyll concentration, wave profile, mineral particles, and whitecaps).

Among these, the sensitivity analysis revealed that only the wave profile significantly influences the bifacial gain. Consequently, for OFPV systems, a rougher sea state, typically represented by a H_s = 3 m, leads to an optimal scenario for the implementation of bifacial modules. However, such gains must be balanced against potential losses generated by sea motion, since these simulations considered a static PV module in the environment.

Bulk contribution resulted in being negligible, as changes in bifacial gain lower than 1% were obtained when going from clear waterbodies to turbid scenarios. Similarly, the effect of whitecaps, while potentially influential due to its high reflectivity spectra, was highly attenuated due to its random distribution, leading to an albedo result dominated mostly by sea water.

Simulations under realistic ocean regimes revealed a seasonal variation in bifacial gain that follows the same pattern of solar irradiance. This is mainly attributed to higher solar altitudes reached in summertime. Nevertheless, this seasonal trend decays at higher latitudes because, in such locations, diffuse radiation becomes more prevalent due to increased air mass. Diffuse radiation, being isotropic and directionless, is less effective for rear-side reflection.

Overall, average bifacial gain values ranging from 5 to 8% were obtained in the four locations selected. Such values can then be used in future analysis of OFPV projects, helping to determine the cost-effectiveness of using bifacial modules by weighing their extra cost against the additional energy generated by them, leading to breakeven or lower LCOE values compared to monofacial scenarios.

5

Conclusion, Research Limitation and Future Recommendations

5.1. Conclusion

This thesis aims to develop, validate, and apply a computational model capable of estimating ocean surface albedo (OSA) for a waterbody. This is to understand its impact on the bifacial gain of offshore floating photovoltaic plants. The motivation of this research was the existing gaps of the current models and their empirical nature, whose location-specific calibrations often restrict their applicability at a global scale.

To achieve this goal, the main thesis is divided into three main chapters, each one of them addressing a different research question. Firstly, a new model was required, and for this, the software GenPro4 was chosen because its function is precisely to simulate the optical response of solar cells under radiation. Therefore, the first research question addresses **how the GenPro4 model can be modified to accurately estimate OSA**, including the effects of air-sea interface as well as the waterbody bulk. Secondly, a validation of this model was needed to assess **how well the results, based on GenPro4, match real measurements of OSA.** Finally, the validated model was applied in different scenarios to evaluate **how OSA changes under different scenarios, and how those changes affect the bifacial gain in offshore floating photovoltaic (OFPV) systems.**

To answer the first research question, in chapter 2, the reflectivity coming from the waterbody was divided into two main categories: interface and bulk reflectivity. While the first one depends on the interface air-water, and therefore, on the wave profile, the bulk reflectivity relies on the organic compounds dissolved in it, neglecting the contribution of backscattering caused by mineral particles. GenPro4 simulations of contrasting scenarios revealed that OSA increases by up to 800% under wavy conditions (H_s = 2 m and T_p = 10 s) compared to a flat water surface. Subsurface contributions to reflectivity were found to be negligible across the spectra, though they do modify the absorption profile of the waterbody.

Despite the existing match between the GenPro4 model and the empirical approach proposed by Séférian, a numerical validation was executed in chapter 3, aiming to respond to the second research question related to how well the proposed model fits with real measured data. This process exposed a lack of spectral accuracy produced by the omission of backscattering in the optical simulation. After including the effect of the latter, the simulations exhibited an accurate fitting with the real data measurements, obtaining maximum RMSE values of 0.72% for clear water datasets and 3.8% for turbid water datasets. Furthermore, the maximum error obtained in the case of turbid waters (3.8%) was under extreme turbid conditions (674g/m^3). For the rest of the datapoints in the sample, the RMSE obtained was below 2%, demonstrating that the model performs robustly under low turbidity conditions typical of offshore environments.

To address the third and final research question, concerning how this dynamic albedo affects the bifacial

gain of OFPV plants, two studies were conducted in chapter 4: a sensitivity analysis and a regional assessment. Sensitivity studies identified wave profile as the dominant variable affecting albedo, and consequently, bifacial gain, with variations up to 3.5% between cases, while the remaining parameters (chlorophyll concentration, mineral particle concentration, and whitecaps) contributed less than 1%. The regional simulations across different locations revealed a clear seasonal variability of bifacial gain. The results showed a pattern of the variable similar to that of irradiance. However, such a pattern weakens at higher latitudes because of the influence of diffuse radiation. Across all analyzed locations, the average bifacial gain ranged between 5 - 8%, suggesting similar energy enhancement potential across diverse oceanic settings.

Overall, this study successfully fulfilled its central objective, providing a physically-based computational tool that enables the dynamic calculation of OSA under varying environmental conditions and quantifying its effect on bifacial PV performance. Chapter 2 demonstrated the feasibility of using the model GenPro4, initially thought for solar cells, in optical simulations at larger scales over wavy water surfaces. Then, chapter 3 offered additional modifications to the tool regarding the effects of backscattering that were initially neglected. Once incorporated, the proposed model showed a strong accuracy with the measured data, validating its robustness. Finally, chapter 4 linked OSA to bifacial gain to assess the potential energy gain under different scenarios, confirming that OSA indeed plays an important role in bifacial gain, leading to changes of up to 3.5% when comparing different sea scenarios.

5.2. Recommendations for Future Work

The main limitation of the proposed model regards the computational cost. Each wave scenario produces a unique reflectivity spectrum, requiring substantial computation time. Since the sea profile changes every second, representing it dynamically remains computationally demanding. Future efforts should aim to reduce computational times for the spectral reflectivity of a certain sea profile. This can be tackled either by optimizing the internal routines of the GenPro4 model or by creating lookup tables of precomputed OSA parametrized by two main variables (H_s and T_p).

A second limitation concerns the integration of the dynamic albedo environment in the PVMD TOOLBOX. Currently, each simulation couples a specific spectral reflectivity distribution with a unique environment, which substantially increases computational time. Decoupling both variables would lead to faster computations and, therefore, the generation of a larger, more comprehensive dataset of bifacial gain results.

Finally, the last obstacle identified regards the validation process. Real measured OSA, or spectral reflectivity, is rarely found for waterbodies, since these expeditions are focused mainly on land applications. The current validation relied on flat-surface assumptions. Future work should therefore include field measurements that explicitly account for sea roughness, enabling more realistic comparisons and further refinement of the model.

References

[1] S. Golroodbari and W. V. Sark, "On the effect of dynamic albedo on performance modelling of offshore floating photovoltaic systems," *Solar Energy Advances*, vol. 2, no. 100016, pp. 1–6, 2022. DOI: 10.1016/j.seja.2022.100016.

[2] G. Tina, F. Scavo, L. Merlo, and F. Bizzarri, "Comparative analysis of monofacial and bifacial photovoltaic modules for floating power plants," *Applied Energy*, vol. 281, p. 116 084, 2021. DOI: 10.1016/j.apenergy.2020.116084.

[3] S. Vasuki, J. Levell, R. Santbergen, and O. Isabella, "A technical review on the energy yield estimation of offshore floating photovoltaic systems," *Renewable and Sustainable Energy Reviews*, vol. 216, p. 115 596, 2025. DOI: 10.1016/j.rser.2025.115596.

[4] R. Frouin, M. Schwindlin, and P. Deschamps, "Spectral reflectance of sea foam in the visible and near-infrared: In situ measurements and remote sensing implications," *Journal of Geophysical Research*, vol. 101, no. C6, pp. 14 361–14 371, 1996. DOI: 10.1029/96JC00629.

[5] C. H. Whitlock, D. S. Bartlett, and E. A. Gurganus, "Sea foam reflectance and influence on optimum wavelength for remote sensing of ocean aerosols," *Geophysical Research Letters*, vol. 9, no. 6, pp. 719–722, 1982. DOI: 10.1029/GL009i006p00719.

[6] A. Kokhanovsky, "Spectral reflectance of whitecaps," *Journal of Geophysical Research: Oceans*, vol. 109, no. C05 021, 2004. DOI: 10.1029/2003JC002177.

[7] K. Moore, K. Voss, and H. Gordon, "Spectral reflectance of whitecaps: Their contribution to water□leaving radiance," *Journal of Geophysical Research: Oceans*, vol. 105, no. C3, pp. 6493–6499, 2000. DOI: 10.1029/1999JC900334.

[8] H. Dierssen, "Hyperspectral measurements, parameterizations, and atmospheric correction of whitecaps and foam from visible to shortwave infrared for ocean color remote sensing," *Frontiers in Earth Science*, vol. 7, p. 14, 2019. DOI: 10.3389/feart.2019.00014.

[9] P. Koepke, "Effective reflectance of oceanic whitecaps," *Applied Optics*, vol. 23, no. 1, pp. 1816–1824, 1984. DOI: 10.1364/AO.23.001816.

[10] J. Wei, T. Ren, P. Yang, S. DiMarco, and E. Mlawer, "An improved ocean surface albedo computational scheme: Structure and performance," *Geophysical Research Oceans*, vol. 126, no. e2020JC016958, 2021. DOI: 10.1029/2020JC016958.

[11] D. Salisbury, M. Anguelova, and I. Brooks, "Global distribution and seasonal dependence of satellite□based whitecap fraction," *Geophysical Research Letters*, vol. 41, pp. 1616–1623, Mar. 2014. DOI: 10.1002/2014GL059246.

[12] M. Albert, M. Anguelova, A. Manders, M. Schaap, and G. de Leeuw, "Parameterization of oceanic whitecap fraction based on satellite observations," *Atmospheric Chemistry and Physics*, vol. 16, pp. 13 725–13 751, 2016. DOI: 10.5194/acp-16-13725-2016.

[13] K. Randolph, H. Dierssen, M. Twardowski, A. Cifuentes-Lorenzen, and C. Zappa, "Novel methods for optically measuring whitecaps under natural wave-breaking conditions in the southern ocean," *Journal of Atmospheric and Oceanic Technology*, vol. 34, no. 3, pp. 533–554, 2017. DOI: 10.1175/JTECH-D-16-0086.1.

[14] R. Aguirre, "Spectral reflectance analysis of the caribbean sea," *Geofísica Internacional*, vol. 5, no. 4, pp. 385–398, 2013. DOI: 10.1016/S0016-7169(14)70073-X.

[15] J. Du, P. Jacinthe, and L. Zhang, "Retrieval of lake water surface albedo from sentinel-2 remote sensing imagery," *Journal of Hydrology*, vol. 617, p. 128 904, 2023. DOI: 10.1016/j.jhydrol.2022.128904.

[16] J. Du, P. Jacinthe, and L. Zhang, “Water surface albedo and its driving factors on the turbid lakes of northeast china,” *Ecological Indicators*, vol. 146, p. 109 905, 2023. DOI: 10.1016/j.ecolind.2023.109905.

[17] X. Yu, Z. Lee, S. Shang, M. Wang, and L. Jiang, “Estimating the water-leaving albedo from ocean color,” *Remote Sensing of Environment*, vol. 269, p. 112 807, 2022. DOI: 10.1016/j.rse.2021.112807.

[18] A. Morel and S. Maritorena, “Bio-optical properties of oceanic waters: A reappraisal,” *Journal of Geophysical Research: Oceans*, vol. 106, no. C4, pp. 7163–7180, 2001. DOI: 10.1029/2000JC000319.

[19] S. Patel and A. Rix, “Water surface albedo modelling for floating pv plants,” in *Proc. 6th Southern African Solar Energy Conf. (SASEC)*, vol. 19, 2019, pp. 1–6.

[20] K. Cheng *et al.*, “Analysis of wind–wave relationship in taiwanwaters,” *Journal of Marine Science and Engineering*, vol. 13, no. 6, p. 1047, 2025. DOI: 10.3390/jmse13061047.

[21] K. Hasselmann *et al.*, *Measurements of wind-wave growth and swell decay during the Joint North Sea Wave Project (JONSWAP)*. Ergänzungsheft zur Deutschen Hydrographischen Zeitschrift, 1973.

[22] C. M. Service. “Copernicus marine service.” (2025), [Online]. Available: https://marine.copernicus.eu/.

[23] L. Donatini, J. Verwilligen, G. Delefortrie, M. Vantorre, and E. Lataire, “Physically accurate real-time synthesis of ocean waves for maritime simulators,” *Applied Ocean Research*, Jan. 2024, Preprint.

[24] Z. Jin, T. Charlock, W. Smith, and K. Rutledge, “A parameterization of ocean surface albedo,” *Geophysical Research Letters*, vol. 31, no. 22, p. L22301, 2004. DOI: 10.1029/2004GL021180.

[25] X. Li *et al.*, “Mapping global ocean surface albedo from satellite observations: Models, algorithms, and datasets,” *Int. Arch. Photogramm. Remote Sens. Spatial Inf. Sci.*, vol. XLII-3, pp. 967–974, 2018. DOI: 10.5194/isprs-archives-XLII-3-967-2018.

[26] N. Earthdata, *Nasa earthdata*, 2025. [Online]. Available: https://www.earthdata.nasa.gov/.

[27] M. Fewell and A. von Trojan, “Absorption of light by water in the region of high transparency: Recommended values for photon-transport calculations,” *Applied Optics*, vol. 58, no. 9, pp. 2408–2421, 2019. DOI: 10.1364/AO.58.002408.

[28] R. Séférian *et al.*, “An interactive ocean surface albedo scheme (osav1.0): Formulation and evaluation in arpege-climat (v6.1) and lmdz (v5a),” *Geoscientific Model Development*, vol. 11, no. 1, pp. 321–338, 2018. DOI: 10.5194/gmd-11-321-2018.

[29] L. Clementson and B. Wojtasiewicz, “Dataset on the absorption characteristics of extracted phytoplankton pigments,” *Data in Brief*, vol. 24, p. 103 875, 2019. DOI: 10.1016/j.dib.2019.103875.

[30] J. C. Larsen and B. R. Barkstrom, *Effects of realistic angular reflection laws for the Earth’s surface upon calculations of the Earth-atmosphere albedo*. Princeton, USA: Science Press, 1977, p. 451.

[31] J. Taylor, J. Edwards, M. Glew, P. Hignett, and A. Slingo, “Studies with a flexible new radiation code. ii: Comparisons with aircraft short-wave observations,” *Quarterly Journal of the Royal Meteorological Society*, vol. 122, no. 532, pp. 839–861, 1996. DOI: 10.1002/qj.49712253204.

[32] R. Santbergen, T. Meguro, T. Suezaki, G. Koizumi, K. Yamamoto, and M. Zeman, “Genpro4 optical model for solar cell simulation and its application to multijunction solar cells,” *IEEE Journal of Photovoltaics*, vol. 7, no. 3, pp. 919–926, 2017. DOI: 10.1109/JPHOTOV.2017.2669640.

[33] T. R. Lee, T. Vander, T. Hill, J. Obelcz, B. Phrampus, and J. Graw, “The updated distribution of clay minerals in the world ocean,” *Marine Geology*, vol. 492, p. 107 695, 2026. DOI: 10.1016/j.margeo.2025.107695.

[34] L. Ma, F. Wang, C. Wang, C. Wang, and J. Tan, “Investigation of the spectral reflectance and bidirectional reflectance distribution function of sea foam layer by the monte carlo method,” *Applied Optics*, vol. 54, no. 4, pp. 878–885, 2015. DOI: 10.1364/AO.54.009863.

[35] R. Sauzède, P. R. Renosh, J. Uitz, and H. Claustre, “Copernicus marine product User manual for MULTIOBS_GLO_BIO_BGC_3D_REP_015_010,” EU Copernicus Marine Service, Toulouse, France, Rep. CMEMS-MOB-PUM-015-010, Nov. 2025, Issue 5.0. [Online]. Available: https://documentation.marine.copernicus.eu/PUM/CMEMS-MOB-PUM-015-010.pdf.

[36] S. Colella, E. Böhm, C. Cesarini, Q. Jutard, and V. E. Brando, “Copernicus Marine product User manual for Ocean colour products,” EU Copernicus Marine Service, Toulouse, France, Tech. Rep. CMEMS-OC-PUM-6.0, Nov. 2025. [Online]. Available: https://documentation.marine.copernicus.eu/PUM/CMEMS-OC-PUM.pdf.

[37] C. D. Mobley, *Light and Water: Radiative Transfer in Natural Waters*. San Diego, CA, USA: Academic Press, 1994.

[38] RAC/SPA – UNEP/MAP, “Management plan of the coastal and marine area of shash – gulf of sirte (libya),” Regional Activity Centre for Specially Protected Areas, UNEP/MAP, Tech. Rep., 2024, Assessment-diagnosis and plan document. [Online]. Available: https://www.rac-spa.org/sites/default/files/doc_imap/mangmt_plan_shash_gulf.pdf.

[39] P. M. Salgado-Hernanz, A. Regaudie-de-Gioux, D. Antoine, and G. Basterretxea, “Pelagic primary production in the coastal mediterranean sea: Variability, trends, and contribution to basin-scale budgets,” *Biogeosciences*, vol. 19, no. 1, pp. 47–69, 2022. DOI: 10.5194/bg-19-47-2022.

[40] V. Echevin *et al.*, “Physical and biogeochemical impacts of rcp8.5 scenario in the peru upwelling system,” *Biogeosciences*, vol. 17, no. 12, pp. 3317–3341, 2020. DOI: 10.5194/bg-17-3317-2020.

[41] X. Li, X. Fan, H. Yan, A. Li, M. Wang, and Y. Qu, “Mapping global ocean surface albedo from satellite observations: Models, algorithms, and datasets,” in *Proc. of the ISPRS TC III Mid□term Symposium “Developments, Technologies and Applications in Remote Sensing”, 7□10 May 2018, Beijing, China*, ser. Int. Arch. Photogramm. Remote Sens. Spatial Inf. Sci. Vol. XLII□3, 2018, pp. 967–970. DOI: 10.5194/isprs-archives-XLII-3-967-2018.

[42] K. A. Casey *et al.*, “A global compilation of in situ aquatic high spectral resolution inherent and apparent optical property data for remote sensing applications,” *Earth System Science Data*, vol. 12, pp. 1123–1139, 2020. DOI: 10.5194/essd-12-1123-2020.

[43] E. Knaeps *et al.*, “The seaswir dataset,” *Earth System Science Data*, vol. 10, pp. 1439–1449, 2018. DOI: 10.5194/essd-10-1439-2018.

[44] X. Yu, Z. Lee, and W. Lai, “Global distribution of the spectral power coefficient of particulate backscattering coefficient obtained by a neural network scheme,” *Remote Sensing of Environment*, vol. 296, p. 113 750, 2023. DOI: 10.1016/j.rse.2023.113750.

[45] C. D. Mobley, Ed., *The Oceanic Optics Book*. Dartmouth, NS, Canada: International Ocean Colour Coordinating Group (IOCCG), 2022, p. 924. DOI: 10.25607/OBP-1710.

[46] A. Morel, D. Antoine, and B. Gentili, “Bidirectional reflectance of oceanic waters: Accounting for raman emission and varying particle scattering phase function,” *Applied Optics*, vol. 41, no. 30, pp. 6289–6306, 2002. DOI: 10.1364/AO.41.006289.

[47] L. Lacour, B. Dewitte, N. B. Chéruy, R. Roehrig, A. J. Bintanja, and F. Hourdin, “An interactive ocean surface albedo scheme (OSAv1.0): Formulation and evaluation in ARPEGE-Climat (V6.1) and LMDZ (V5A),” *Geoscientific Model Development*, vol. 11, no. 1, pp. 321–339, Jan. 2018. DOI: 10.5194/gmd-11-321-2018. [Online]. Available: https://gmd.copernicus.org/articles/11/321/2018/.

[48] C. Roesler and M. Perry, “In situ phytoplankton absorption, fluorescence emission, and particulate backscattering spectra determined from reflectance,” *Journal of Geophysical Research: Oceans*, vol. 100, no. C7, pp. 13 279–13 294, 1995. DOI: 10.1029/95JC00455.

[49] M. Twardowski, E. Boss, J. Sullivan, and P. Donaghay, “Modeling the spectral shape of absorption by chromophoric dissolved organic matter,” *Marine Chemistry*, vol. 89, no. 1–4, pp. 69–88, 2004. DOI: 10.1016/j.marchem.2004.02.008.

[50] B. Nechad, K. G. Ruddick, and Y. Park, “Calibration and validation of a generic multisensor algorithm for mapping of total suspended matter in turbid waters,” *Remote Sensing of Environment*, vol. 114, no. 4, pp. 854–866, Apr. 2010. DOI: 10.1016/j.rse.2009.11.022.

[51] M. R. Vogt *et al.*, “Introducing a comprehensive physics-based modelling framework for tandem and other pv systems,” *Solar Energy Materials and Solar Cells*, vol. 247, p. 111 944, Sep. 2022. DOI: 10.1016/j.solmat.2022.111944.

[52] EE Renewables, *Bifacial vs monofacial solar panels: Benefits & costs 2025*, https://www.eerenewables.co.uk/solar-guides/bifacial-vs-monofacial-solar-panels/, Accessed: Feb. 02, 2026, 2025.

[53] Copernicus Climate Change Service (C3S), “ERA5 hourly data on single levels from 1940 to present,” 2023. DOI: 10.24381/cds.adbb2d47.

A

Backscattering vs Absorption Map

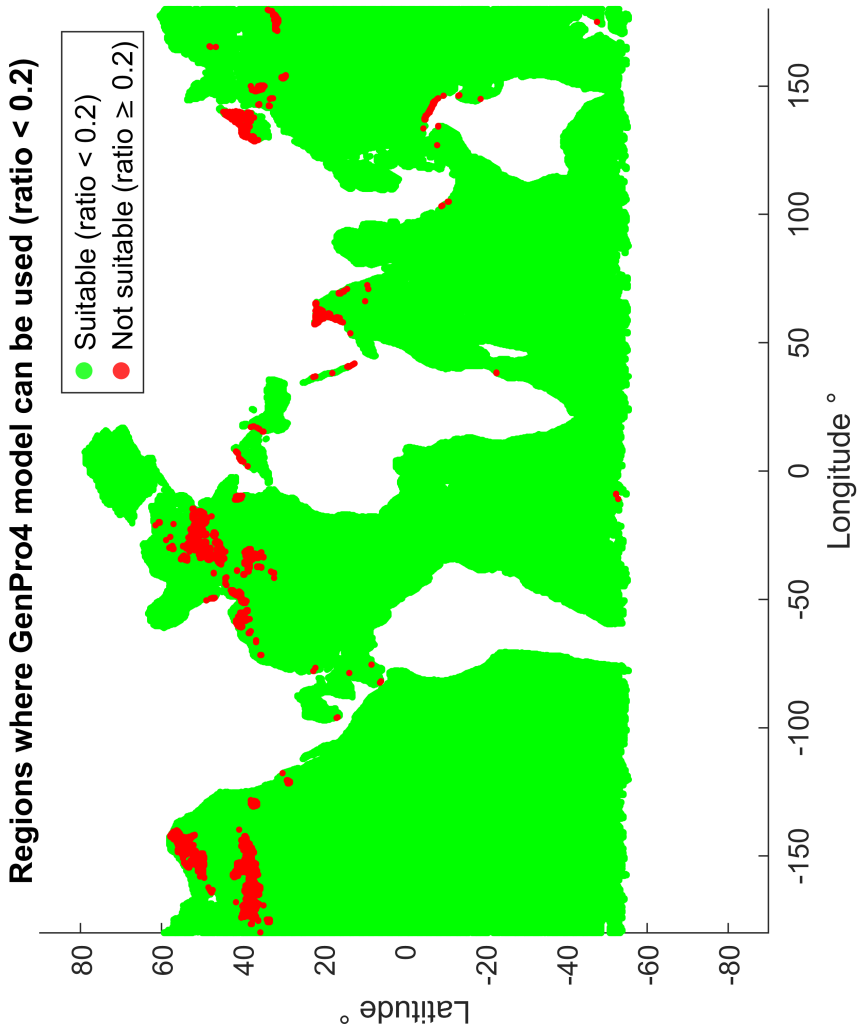

B

OSA datasets

B.1. Global datasets

In [41], three main global datasets that register measurements of Ocean Surface Albedo are discussed. The details of the data quality of each dataset are present in Table B.1.

Name	Spatial Coverage	Temporal Span	Spatial Resolution	Sampling Frequency
CLARA-A1	Global	1982-2009	25km	5days-1month
TCOWA	Global Ocean Surface	2011	1km	daily
GLASS phase-2	Global	2000-2013	1km	8 days

Table B.1: List of current worldwide OSA datasets [41]

- CLARA-A1: The cloud, albedo and radiation (CLARA) is a global dataset generated by the usage of satellite applications used on climate monitoring. It has a relatively coarse spatial resolution of 25km which is not ideal considering that the length scale of offshore PV plants is less than a kilometer. Besides, the Ocean Surface Albedo in this dataset is set to a constant value of 0.0676 due to the unavailability of wind speed and chlorophyll data.
- TCOWA: This dataset is generated from an albedo-estimator algorithm called MODIS, which takes as main input parameters the chlorophyll content, wind speed and wind direction. Therefore, it also includes the effects of subsurface reflection. Nevertheless, this model has two main drawbacks. (a) It is a reanalysis product, meaning that it does not offer real measurements of the variable of interest, but it calculates it based on related parameters. On the other hand, the temporal span is only one year which limits the posibilities of comparison.
- GLASS phase-2: This product was also generated via MODIS algorithm which reduces its reliability for not being an in-site measurement type of product, even when its temporal span is higher (13 years). This model was thought originally for in-land purposes, but the second version of it includes portions of the ocean instead of full coverage, which also represents an important limitation if we use it as a validation dataset.

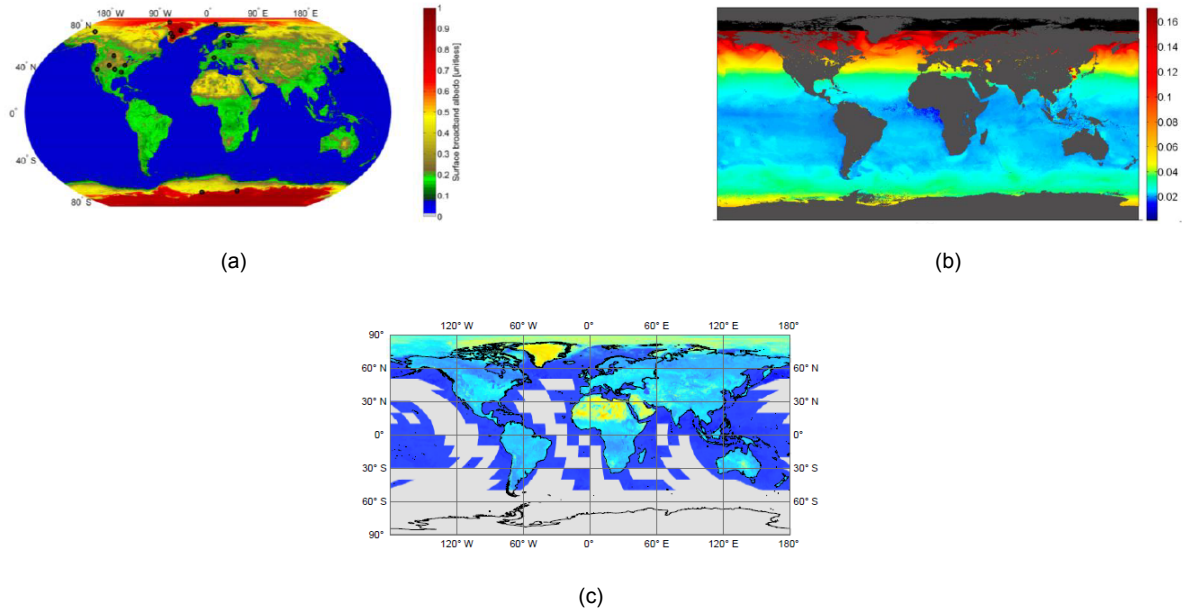

(a) (b)

(c)

Figure B.1: Color-plot of albedo for:(a) CLARA-A1, (b) TCOWA and (c) GLASS phase-2. Extracted from [41].

B.2. BIOSOPE dataset (clear waters)

BIOSOPE is a multidisciplinary cruise that gathered investigators from different fields with the aim of measuring the most relevant IOP and AOP for ocean waters.

Among all the researchers in this expedition, the work carried out by Sramsky and Reynolds is very useful for this research because of the parameters measured. In this cruise, the values of the absorption coefficient of the main organic substances dissolved in water (CDOM, NAP, and chlorophyll), the backscattering coefficient of particles, and the overall spectral reflectivity are measured. Most of the data is available in a spectral range going from 300 nm to 900 nm. Nevertheless, for the case of the backscattering coefficient, its value is only available for the wavelengths 394, 420, 442, 470, 510, 532, 550, 589, 640, 730, and 852 nm. Then, for the validation process, it is necessary to interpolate the values of backscattering (b_b) over the whole wavelength range.

The methodology adopted by Sramsky and Reynolds is the following. At each coordinate of the expedition, a buoy is located with two radiometers. One of them is placed on top of the buoy to measure the downwelling irradiance at the air-sea interface, which is already attenuated by atmospheric effects. The other radiometer is located 20cm below the sea surface to ensure that the measurements are not influenced by dynamic changes due to sea motion. An illustration of the above mentioned is depicted in Figure B.2.

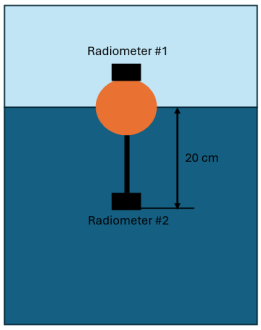

Figure B.2: Illustration of buoys and radiometers employed in Sramsky and Reynolds expedition.

As the measurements of the second radiometer are not taken exactly below the surface, further correction is needed to go from $L_u(20^-)$ to $L_u(0^-)$. In the data processing step, corrections due to absorption in those 20cm are applied to obtain the target variable of upwelling irradiance just under sea surface. This is why the variable is called $L_u(0^-)$ to distinguish it from upwelling irradiance measured above surface that is represented by $L_u(0^+)$. Then, for this specific expedition, we are going to have a dataset of 21 locations (samples) where spectral reflectivity is measured in the range 300-800 with an interval of 2 nm for each measurement.

B.3. SeaSWIR dataset (turbid waters)

In this dataset, a total of 5 sampling campaigns were carried out, where upwelling irradiance measured just over sea level $L_u(0^+)$, downwelling irradiance measured just over sea level $L_d(0^+)$, and total suspended material concentration was collected.

The downwelling irradiance was obtained using a radiometer placed perfectly horizontal, avoiding nearby objects to prevent undesired shadows. The total upwelling radiance from the water considers both effects, upwelling water-leaving radiance and the radiance reflected at the interface. Therefore, it represents a better dataset compared to the BIOSOPE expedition, because its output is the same as GenPro4. The instrument set up to register upwelling and downwelling radiance is shown in Figure B.3

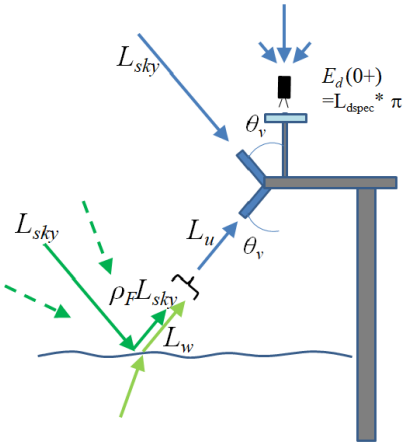

Figure B.3: Emeasurement equipment set up in SeaSWIR expedition. Extracted from [43]

Regarding the concentration of suspended matter, special filters were used during the different campaigns, able to tolerate the high concentrations present in the waterbodies. Such filters were placed into bottles and sunk to the same depth to have even measurement conditions despite the distance between the different locations.

C

PVMD TOOLBOX Code Ajustments

To adapt the PVMD TOOLBOX to work with spectral reflectivity values, the procedure used to define the simulation of the environment must be changed. In particular, the section of the code responsible for the environment associated with MODULE_main must be updated, as shown in Figure 4.1.

The PVMD TOOLBOX contains an internal code called 'generate_environment.m', which provides the parameters required to define the surrounding environment that interacts optically with the PV modules tested. Accordingly, a specific geometry is generated and discretized into a set of coordinates in three-dimensional space. These points are interconnected to form the faces of the geometry, typically using triangles or quadrilaterals, as these shapes require the fewest points. Each face is assigned optical properties to estimate the overall surface reflectivity of the environment. In particular, the outputs of this code ('generate_environment.m') are:

- **Albedo**: It corresponds to a matrix of size 1×1, where the cell value corresponds to the overall Albedo at the surface.
- **F**: It defines the data points of each face. Therefore, if n is the number of faces in the geometry, F is a matrix of order $n \times 3$ when the faces are defined as triangles, and $n \times 4$ when quadrilaterals are used.
- **Materials**: It is a matrix of size $n \times 1$, where every element specifies the material assigned to a given face.
- **OPA**: It defines the opacity (transparency) of each face in the environment. Consequently, it is a matrix of order $n \times 1$.
- **RGB**: It defines the color of each face in the environment. It is a matrix of size $n \times 3$, where each column represents the saturation of the R (red), G (green), and B (blue) components that define a specific color.
- **Scattering**: It is a binary matrix of order $n \times 1$, where 0 represents a specular reflection (no scattering), and 1 corresponds to Lambertian reflection (complete, direction-independent scattering).

To incorporate the spectral reflectivity generated in GenPro4, only the **Albedo** needs to be modified, since the remaining components are related to the geometry definition or to the color and transparency chosen for visualization, and are not directly related to surface reflectivity. In addition, bulk reflectivity must be added to account for the overall optical effect of the waterbody. Therefore, the required modifications to this input code are related to integrating the subsurface reflectivity and to transforming the Albedo variable into a spectral parameter, changing it from a 1×1 matrix to $1 \times m$, where m represents the resolution of the wavelength range chosen for simulation.

Then, when running the 'generate_environment.m' code, the following inputs are required.

- 'Select wave profile.mat': Here, the file (with a .mat extension) containing the wave height map must be loaded.

- 'Select your Reflectivity Spectrum.mat': In this case, the spectral reflectivity data generated by GenPro4 must be loaded.
- 'Select database.mat': This file will consist of an array of size $t \times 4$, where t is the time lapse chosen in the simulation, and the 4 columns represent the following coefficients.
  - **Chlorophyll concentration** (mg/m^3), extracted from [36]. The absorption coefficient spectrum is calculated by multiplying the chlorophyll concentration by the absorption spectrum given in [29]
  - **Backscattering coefficient of mineral particles** at 680nm (m^{-1}), extracted from [36]. The overall spectrum of this coefficient is obtained using Equation 3.6
  - **Absorption coefficient of CDOM** at 440nm (m^{-1}), extracted from [36]. As in the previous case, the corresponding spectrum for this coefficient is obtained using Equation 3.10.
  - **Whitecap contribution**: the model requires the mean wind speed at the study location. Wind speed data are collected from [53], and the whitecap coverage fraction is computed using Equation 1.14.

With these input parameters already defined in the code, the overall reflectivity, including the effects at the surface and the bulk of the waterbody, is calculated using Equation 3.8 and Equation 3.9. As a result, the albedo output is a $1 \times m$ vector, where each considered wavelength has a different reflectivity value.